

Near Source Energy Partitioning for Regional Waves in 2D and 3D Models

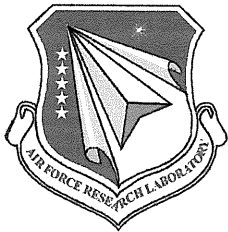
**Xiao-Bi Xie
Thome Lay
Ru-Shan Wu**

**University of California, Santa Cruz
1156 High Street
Santa Cruz, CA 95064**

Final Report

30 April 2008

<p>APPROVED FOR PUBLIC RELEASE; DISTRIBUTION UNLIMITED.</p>
--



**AIR FORCE RESEARCH LABORATORY
Space Vehicles Directorate
29 Randolph Road
AIR FORCE MATERIEL COMMAND
Hanscom AFB, MA 01731-3010**

NOTICE AND SIGNATURE PAGE

Using Government drawings, specifications, or other data included in this document for any purpose other than Government procurement does not in any way obligate the U.S. Government. The fact that the Government formulated or supplied the drawings, specifications, or other data does not license the holder or any other person or corporation; or convey any rights or permission to manufacture, use, or sell any patented invention that may relate to them.

This report was cleared for public release and is available to the general public, including foreign nationals. Qualified requestors may obtain additional copies from the Defense Technical Information Center (DTIC) (<http://www.dtic.mil>). All others should apply to the National Technical Information Service.

AFRL-RV-HA-TR-2008-1067 HAS BEEN REVIEWED AND IS APPROVED FOR
PUBLICATION IN ACCORDANCE WITH ASSIGNED DISTRIBUTION STATEMENT.

//Signature//

ROBERT RAISTRICK
Contract Manager

//Signature//

PAUL TRACY, Acting Chief
Battlespace Surveillance Innovation Center

This report is published in the interest of scientific and technical information exchange, and its publication does not constitute the Government's approval or disapproval of its ideas or findings.

REPORT DOCUMENTATION PAGE				Form Approved OMB No. 0704-0188	
Public reporting burden for this collection of information is estimated to average 1 hour per response, including the time for reviewing instructions, searching existing data sources, gathering and maintaining the data needed, and completing and reviewing this collection of information. Send comments regarding this burden estimate or any other aspect of this collection of information, including suggestions for reducing this burden to Department of Defense, Washington Headquarters Services, Directorate for Information Operations and Reports (0704-0188), 1215 Jefferson Davis Highway, Suite 1204, Arlington, VA 22202-4302. Respondents should be aware that notwithstanding any other provision of law, no person shall be subject to any penalty for failing to comply with a collection of information if it does not display a currently valid OMB control number. PLEASE DO NOT RETURN YOUR FORM TO THE ABOVE ADDRESS.					
1. REPORT DATE (DD-MM-YYYY) 30-04-2008		2. REPORT TYPE Final Report		3. DATES COVERED (From - To) 01-04-2005 to 30-03-2008	
4. TITLE AND SUBTITLE Near Source Energy Partitioning for Regional Waves in 2D and 3D Models				5a. CONTRACT NUMBER FA8718-05-C-0021	
				5b. GRANT NUMBER	
				5c. PROGRAM ELEMENT NUMBER 62601F	
6. AUTHOR(S) Xiao-Bi Xie, Thorne Lay and Ru-Shan Wu				5d. PROJECT NUMBER 1010	
				5e. TASK NUMBER SM	
				5f. WORK UNIT NUMBER A1	
7. PERFORMING ORGANIZATION NAME(S) AND ADDRESS(ES) University of California, Santa Cruz 1156 High Street Santa Cruz, CA 95064				8. PERFORMING ORGANIZATION REPORT NUMBER	
9. SPONSORING / MONITORING AGENCY NAME(S) AND ADDRESS(ES) Air Force Research Laboratory 29 Randolph Rd. Hanscom AFB, MA 01731-3010				10. SPONSOR/MONITOR'S ACRONYM(S) AFRL/RVBYE	
				11. SPONSOR/MONITOR'S REPORT NUMBER(S) AFRL-RV-HA-TR-2008-1067	
12. DISTRIBUTION / AVAILABILITY STATEMENT Approved for Public Release; Distribution Unlimited.					
13. SUPPLEMENTARY NOTES					
14. ABSTRACT The complex excitation and energy partitioning mechanisms yielding regional phases are difficult to empirically separate by data analysis. Thus, numerical modeling approaches are valuable for investigating excitation and propagation of regional seismic phases. We use accurate full-wave simulations (2D and 3D finite-difference method, and 2D boundary element method) to calculate seismic wave excitation and propagation in near-source region. An embedded array slowness analysis is used for quantifying how energy will be partitioned into the long-range propagation regime. Due to its high efficiency, the method can simulate near-source processes using very fine structures. A large number of source and model parameters can be examined for broad frequency ranges. We use this method to investigate the effect of volumetric and topographic scattering on the near-source energy partitioning for an explosion source. Different random velocity fluctuations and topographic models, variable source depth, and different Q models are investigated using numerical simulations. The responses of different phases as functions of frequency and source/model parameters are calculated and their energy budget evaluated.					
15. SUBJECT TERMS Synthetic seismograms, Seismic scattering, Seismic phases					
16. SECURITY CLASSIFICATION OF:			17. LIMITATION OF ABSTRACT SAR	18. NUMBER OF PAGES 58	19a. NAME OF RESPONSIBLE PERSON Robert Raistrick
a. REPORT UNC	b. ABSTRACT UNC	c. THIS PAGE UNC			19b. TELEPHONE NUMBER (include area code) 781-377-3726

Table of Contents

1	Summary	1
2	Introduction	2
3	Methodology	4
	3.1. The Near-Source Strategy	4
	3.2. Local Slowness Analysis	4
	3.3. The Energy Partitioning Formalism	8
	3.4. Testing the Validity of the Method	10
4	Regional Phase Excitation: Contributions from Volumetric Scattering	13
	4.1. <i>P</i> - <i>pS</i> -to- <i>Lg</i> and <i>P</i> -to- <i>Lg</i> Conversion	13
	4.2. Contributions from the <i>S</i> *-Wave	17
	4.3. The Frequency Dependent <i>Lg</i> Excitation Function	18
5	Regional Phase Excitation: Contributions from Surface Scattering	22
	5. 1. Phenomena Resulting from Free Surface Scattering	22
	5. 2. Contributions of Free Surface Scattering to <i>Lg</i> -Wave Excitation	26
	5. 3. Effect of free surface roughness	27
	5. 4. The Effect of Source Depth	29
	5. 5. The Effect of Correlation Length	30
	5. 6. The Effect of Intrinsic Attenuation	31
	5. 7. Variance of Statistical Results	32
6	Regional Phase Excitation: Scattering in Three-Dimensions	34
	6. 1. The Volumetric Scattering and the Excitation of SH Component	34
	6. 2. Simulating the Rough Free Surface Scattering in 3D Model	37
	6. 3. The Effect of 3D Surface Scattering	39
7	Conclusion	43
	References	45

List of Figures

- Figure 1.** Slowness domain display with (a) energy distribution in 2D slowness domain, and (b) energy distribution in mixed horizontal slowness and depth domain. Vertical lines indicate the upper-mantle S -slowness p_{SM} . Circles and dashed lines denote crustal P -wave slowness p_P and S -wave slowness p_S . Energy falling to the right of upper-mantle S -slowness can be trapped in the waveguide and contribute to Lg . 6
- Figure 2.** Configuration for using the FDSA method to investigate near-source processes. 7
- Figure 3.** Example of slowness analysis at 180 km distance. 7
- Figure 4.** Slowness analysis calculated for the EK model and EK model with random patches at different depths. Column (a) is for frequency band 0.3-1.5 Hz and (b) is for 2.0-5.0 Hz. The top row is for background velocity model and the lower rows are for models with random patches. The depths of random patches are labeled in the panels. Details see the text. 8
- Figure 5.** Comparison between waveguide energy flux at 180 km (left column) and the wave energy on the surface at 450 km (right column) for Pg , Lg and Rg windows. The frequency range is 0.3-1.2 Hz. Shown in each panel is relative energy versus the depth of random patches. Dashed lines indicate the energy level for background model and short bars indicate the energy changes due to the near-source scattering. 10
- Figure 6.** Examples showing the slowness analyses at distances (a) 50 km and (b) 100 km. The p_{SM} , p_P and p_S are upper-mantle S -slowness, crustal P -slowness and S -slowness, respectively. The energy that can be trapped in the crustal waveguide is indicated in the figure. 12
- Figure 7.** Comparison between trapped waveguide energy measured at 50 km (horizontal coordinate) and 100 km (vertical coordinate) for frequency bands 0.5-1.5 Hz, 1.0-3.0 Hz and 2.0-4.0 Hz. Different dots are results from different velocity models and source depths. The results show a general linear relationship for all frequencies. 12

Figure 8. P - pS -to- Lg conversion due to shallow scattering. (a) is for the EK-model and (b) is for the EK-model with a shallow random patch. The random patch has a 5% RMS velocity fluctuation and is shown as a shaded area between horizontal distances 5 to 15 km and depths 0 to 2.5 km. The snapshots and results of slowness analyses of P , pS and pS -coda are shown in the figure. Details are given in the text. 14

Figure 9. Horizontal slowness analyses for investigating the P - pS -to- Lg coupling with (a) the EK-model, (b) the EK-model plus a 3% shallow random patch and (c) the EK-model plus a 5% random patch. The p_{SM} , p_P and p_S are upper-mantle S -slowness, crustal P - and S -slowness, respectively. The slowness analyses are conducted at distance 20 km and for depth range 0 to 12.5 km. The configuration of the source and model is the same as that used in Figure 8. Major phases are labeled in the figure and energy circled by dashed rectangles is scattered pS -wave. 15

Figure 10. The P - pS -to- Lg conversion due to a deeper random patch. The random patch has a 3% RMS velocity fluctuation and is shown as a shaded region between distances 5 and 15 km and depths 2.5 and 10 km. The slowness analysis for P , P -coda, pS and pS -coda are also shown in the figure. 16

Figure 11. Energy distribution in depth and horizontal slowness domain for (a) the EK-model, (b) EK-model plus a 3% random patch and (c) EK-model plus a 5% random patch. The configuration of the source and model is same as that used in Figure 10. Energy circled by dashed rectangles is P - pS -to- Lg scattering and energy circled by dashed ellipses is P -to- Lg scattering. 16

Figure 12. Wavefield snapshots for explosion sources at depths (a) 0.5 km and (b) 3.0 km. Note that a shallower explosion is a more efficient source for generating S^* and Rg -waves. 17

Figure 13. Slowness analysis for investigating S^* -to- Lg conversion. Different rows are for different source depths. Dashed rectangles indicate the time-space-slowness windows used to pick the S^* energy. 18

Figure 14. Normalized Lg excitation spectra for sources in different velocity models and at different depths with (a) a model with a homogeneous crust and (b) the EK-model. 19

Figure 15. Normalized Lg excitation spectra for sources in the EK-model with shallow random patches, for (a) the EK-model with a 3% shallow random patch, (b) the EK-model with a 5% shallow random patch, (c) and (d) the isolated scattered energy in (a) and (b) respectively due to the random patches found by removing the energy for the layered models. Note different vertical scales are used for scattered energy. 20

Figure 16. Normalized Lg excitation spectra for sources in the EK-model with deep random patches, for (a) the EK-model with a 3% deep random patch, (b) EK-model with a 5% deep random patch, (c) and (d) the isolated scattered energy in (a) and (b) due to the random patches. 21

Figure 17. Configuration of the source, model and receiver array. 22

Figure 18. Wavefield snapshot at $t = 10.0$ s for a model with random free surface fluctuation, where (a) and (b) are horizontal and vertical components of the wavefield, and (c) and (d) are horizontal and vertical components of the scattered wavefield obtained by subtracting the flat model wavefield from the random surface wavefield. The source is at 20 km horizontal position and 0.5 km depth. 23

Figure 19. Slowness analysis results in the depth-slowness domain for discrete time intervals as the wave sweeps through the observing array for models with different source depths and free surface parameters. The frequency band is between 1.5 Hz and 4.5 Hz. All the panels are normalized in the same scale. In each small figure, the horizontal coordinate is horizontal slowness and the vertical coordinate is depth. The thick vertical line indicates the upper mantle S-wave slowness which separates energy that leaks out of the waveguide (to the left) from energy trapped in the wave guide (to the right) that forms Lg . The PP, PS and PSM are crustal P-wave, S-wave and upper mantle S-wave slownesses, with their values are 0.154, 0.28 and 0.22 s/km, respectively. 24

Figure 20. Slowness analysis results for models with different rms topographic fluctuations. The source depth is 0.5 km. In each time frame the horizontal coordinate is the horizontal slowness and vertical coordinate is the depth. The Rg energy is located near the surface, with slowness similar to the S -wave. 26

Figure 21. Responses as functions of frequency and rms free surface fluctuations. Top row: the near source responses of direct Rg , scattered Rg and the Lg -waves, with (a) R^{Rg_direct} , (b) R^{Rg_scatt} and (c) R^{Lg} . Bottom row: the contributions of surface scattering to these responses, with (d) $R^{Rg_direct} - R_F^{Rg_direct}$, (e) $R^{Rg_scatt} - R_F^{Rg_scatt}$ and (f) $R^{Lg} - R_F^{Lg}$. Note, a negative vertical coordinate is used in (d), where the prisms with solid black tops are below zero plane, while prisms with open tops are above the zero plane. 27

Figure 22. Similar to Figure 4 except each panel is for a different source depth. 29

Figure 23. Similar to Figure 5, except responses are functions of frequencies and source depths. The rms surface fluctuation is 0.15 km, with correlation length 0.5 km. 30

Figure 24. Similar to Figure 4 except each panel is for a model with different correlation distance.	31
Figure 25. Similar to Figure 5, except responses are functions of frequencies and correlation lengths.	32
Figure 26. Net scattered Lg-energy as a function of normalized scale factor ka .	33
Figure 27. Similar to that shown in Figure 4, except a low Q top layer is used in the simulation. To facilitate comparison, the same vertical scale as in Figure 4 is used here.	33
Figure 28. Top row: Responses as functions of frequencies and different random realizations, for (a) direct Rg -wave, (b) scattered Rg -wave and (c) Lg -wave. The bottom row shows response spectra from individual realizations, their mean values and standard deviations.	34
Figure 29. Cartoon showing the configuration of the 3D velocity model, source, and receiver array.	34
Figure 30. Wavefield snapshot for the layered background model (left) and a laterally heterogeneous model with 7% RMS random fluctuations. Shown here is the vertical component of the displacement field.	35
Figure 31. Comparison between synthetic seismograms and energy distribution in horizontal slowness domain for the layered velocity model (left panel) and velocity model with 7% RMS velocity fluctuations (right panel). Receivers are located at depth 1 km. All three components of the seismograms are normalized jointly but the slowness distribution for the radial component of the P-wave has been multiplied by a factor of 0.1. The P and Rayleigh waves can be clearly seen from the radial and vertical components. Note that the tangential component for the layered model is zero. For the random velocity model, scattered waves in both the tangential and vertical components can be seen. Note that much scattered energy falls outside of the upper mantle slowness (dash line circle) and can be trapped into the crustal wave guide to form the Lg wave.	35
Figure 32. The wave energy distribution in the 2D horizontal slowness domain for the vertical (left) and tangential (right) components. The receiver array is located at epicentral distance 28 km and depth 7 km. Note the energy distribution outside of the upper mantle S-wave velocity.	36
Figure 33. The 3D velocity model including both irregular free surface and volumetric heterogeneity. The rough topography is located between distances 5 km and 15 km. The volumetric heterogeneity is located between distances 5 km and 15 km, and between depths 1 km and 5 km. The synthetic seismograms are collected from a 3D array. Shown in the figure is one quarter of the model.	37

Figure 34. Snap shots for an explosion source in different velocity models. Rows (a) to (d) are for a layered model, a layered model with volumetric random velocity fluctuation, a layered model with irregular topography, and a layered model with both volumetric heterogeneity and random topography. The three columns are for x-, y- and z-components.	38
Figure 35. Synthetic seismograms for (a) a layered crust model, (b) a layered model with Gaussian rough free surface; and c) a layered model with exponential rough free surface. All seismograms are normalized with the same scale.	40
Figure 36. Synthetic seismograms and slowness analysis for (a) a layered crustal model and (b) a layered model with rough free surface and volumetric heterogeneity. The model geometry is shown in Figure 33.	41
Figure 37. Wave energy in horizontal slowness and depth domain in the EK model.	41
Figure 38. Wave energy in horizontal slowness and depth domain in EK model plus free surface rough topography. The random free surface has an exponential power spectrum.	42

List of Tables

Table 1. Eastern Kazakh Model	9
Table 2. Three-layer velocity model	23
Table 3. Two-layer velocity model	23
Table 4. Source and model parameters used in numerical simulations	25
Table 5. Normalized energy E/E_0 for Rg and Lg waves in different random surface models.	42

1. SUMMARY

The complex excitation and energy partitioning mechanisms yielding regional phases are difficult to empirically separate by data analysis. Thus, numerical modeling approaches are valuable for investigating excitation and propagation of regional seismic phases. We use accurate full-wave simulations (2D and 3D finite-difference method, and 2D boundary element method) to calculate seismic wave excitation and propagation in the near-source region. An embedded array slowness analysis is used for quantifying how wavefield energy will be partitioned into the long-range propagation regime. Due to its high efficiency, the method can simulate near-source processes using very fine structures. A large number of source and model parameters can be examined for broad frequency ranges. We use this method to investigate the effect of volumetric and topographic scattering on the near-source energy partitioning for an explosion source. Different random velocity fluctuations and topographic models, variable source depth, and different Q models are investigated using numerical simulations. The responses of different phases as functions of frequency and source/model parameters are calculated and their energy budget evaluated.

The results reveal that the depth of the source and the depth of the scattering process have strong effects on P-to-S conversion and partitioning of energy into trapped or leaking signals. The modeling shows that S*-to-Lg excitation is generally stronger for low-frequencies and shallow source depths while P-pS-to-Lg scattering is stronger for high-frequencies. The free surface scattering has strong effect on near source energy partitioning. The scattering process can excite the Rg-wave for a moderately rugged topography, but prevents the formation and propagation of short period Rg-waves when the surface becomes too rugged. For models with a high velocity shallow crust, the free surface scattering provides an important mechanism that transfers energy for an explosion source into the Lg-wave in the near source region. At lower frequencies and for a moderately rugged free surface, the Rg-to-Lg transfer is relatively efficient. At higher frequencies and for a very rugged free surface, the body-to-Lg transfer may dominate the process. The correlation length of the random free surface fluctuation imparts specific frequency dependence to the transfer function, with maximum coupling near $ka=1$. Intrinsic attenuation within the uppermost crust has a strong effect on the energy transfer through surface scattering, with high frequency content losing energy faster than the lower frequency waves.

We expand our simulation and analysis to fully 3D models with both volumetric heterogeneity and rough free surface. Investigating the near source process in 3D is more realistic because it gives correct scattering pattern and geometric spreading. In addition, a general 3D model provides the coupling between the P-SV and SH waves. Velocity models with different volume heterogeneities and surface fluctuations are tested and compared. For an isotropic explosion source in a typical layered model with high velocity top layer, only weak Lg wave (trapped guided wave) can be generated from the S* phase. There is no energy in the tangential component. When adding volume heterogeneities or surface fluctuations in the model, the energy transfers from leaky mode to trapped guided

waves as well as from P-SV mode to the SH mode. For the surface scattering, an exponential random surface fluctuation provide stronger coupling than a Gaussian random surface model. Generally, a model with more small scale topographic fluctuations tends to generate more trapped energy.

2. INTRODUCTION

With the current emphasis on global monitoring for low-yield nuclear tests, regional seismic phases such as *Lg* have become very important for magnitude and yield estimation of underground nuclear tests. (e.g., Nuttli, 1986; Xie, et al., 1996; Patton, 2001). In addition, various *P/S*-type amplitude ratios for high frequency regional phases (e.g., *Pn/Sn*, *Pn/Lg*, *Pg/Lg*, *Pg/Sn*) have become important for event discrimination (e.g., Taylor et al., 1989; Kim et al., 1993, 1997; Walter et al., 1995; Fisk et al., 1996; Taylor, 1996; Taylor and Hartse, 1997; Hartse et al., 1997; Fan and Lay, 1998a-c; Xie, 2002; Bottone et al., 2002). The applications of regional phases for yield estimation and event discrimination are largely based on empirical approaches, and while very promising in many cases, there are major questions about the nature of excitation of *S*-wave dominated phases such as *Lg*. There are similar questions regarding the relative excitation effects for *P/S*-type ratios in regional phases, particularly given the huge scatter observed in both earthquake and explosion data populations.

There are now many observational and theoretical studies addressing the regional phase energy partitioning issue in both the near-source environment and the propagation-path environment. Along the propagation path, the existence of small-scale heterogeneities in the crust and the associated seismic wave scattering has long been addressed by seismologists (Wu and Aki, 1988; Sato and Fehler, 1998), and its effect on the long-range energy partitioning has been documented (Wu, et al., 2000a, b). In the source region, several possible near-source energy excitation mechanisms have been proposed, including *P*-to-*Lg* scattering, *pS*-to-*Lg* conversion at the free surface, *Rg*-to-*Lg* coupling, *S**-to-*Lg* conversion, spall excitation of *S*, tectonic release, explosion asymmetry (CLVD component) and rock-damage (e.g., Day and McLaughlin, 1991; Gupta et al., 1992, 1997; Wallace, 1991; Gutowski, et al., 1984; Lilwall, 1988; Xie and Lay, 1994; Vogfjord, 1997; Johnson and Sammis, 2001).

Due to the complex excitation and energy partitioning processes associated with regional phases, it is difficult to empirically separate the contribution of individual energy partitioning mechanisms by analysis of data. Numerical modeling approaches are thus of great importance for investigating the excitation and propagation of regional phases. Kennett and Mykkeltveit (1984) and Kennett (1989) used the coupled mode method to calculate *Lg*-wave propagation in crustal waveguides with weak lateral heterogeneities. Xie and Lay (1994) investigated *Lg*-wave excitation using the full-wave finite-difference method. Jih (1995, 1996) investigated *Rg*-to-*Lg* coupling as a possible *Lg* excitation mechanism. With an anelastic FD method, Bradley and Jones (1998, 1999) investigated *Lg* propagation and attenuation in Western China and India. Recently, using the 2D and 3D general Fourier methods, Bonner et al. (2003) investigated *Rg* and *Lg* generation, and

partially reproduced the observed spectrum from the Depth of Burial Experiment. Stevens et al. (2003, 2005), and Myers et al. (2005) investigated the physical basis of explosion generated *S*-waves using a 2D nonlinear FD method, which handles axisymmetric near-source effects including spall, cracking, and nonlinear deformation.

The main disadvantages of these numerical methods are their low computation efficiency and huge computer memory requirement, especially when applied to investigate broadband *Lg* excitation. For the purpose of small nuclear test monitoring, the range of interest for *Lg*-wave simulation involves a broad frequency band (0.2 to 10 Hz) and long propagation distances (up to 1000 km or more). At the same time, factors that control the source energy partitioning depend on the detailed source mechanism and fine near-source velocity structure. In addition, there are multiple mechanisms that may potentially contribute to the energy partitioning process. Numerous parameters need to be tested to investigate the characteristics of these mechanisms, especially their contributions to the frequency dependent features of observable discriminants. If random heterogeneities are to be considered, as is likely to be important for high frequency signals, the results have to be calculated statistically from simulations using a large number of realizations. These factors limit the approach of complete FD synthesis of distant waveforms for actual recording geometries.

Although there are continuing controversies about the dominant *P*-to-*S* transfer mechanisms affecting regional phases, most investigators agree that appreciable energy from explosion sources is converted to *S*-waves in the near-source region (e.g., Myers et al., 2003). The physical processes by which an explosion source generates regional phases can be described as energy partitioning taking place in the near-source region. The partitioned energy subsequently propagates through a long waveguide, where secondary energy partitioning effects may occur, but these are less affected by the type of source involved. If the propagation effect is not of primary interest, it is desirable to avoid calculating the immensely time-consuming long-distance propagation part of the problem. In order to focus on the near-source energy partitioning processes, we developed a method which uses accurate full-wave simulation in the near-source region which is followed by a local slowness analysis. This method investigates energy partitioning right at the source region, but quantifies how energy will transfer into the long range propagation path, which is critical for comparisons with data. The localized analysis thereby isolates the physical processes controlling the energy partitioning.

In the following sections, we first present the method with numerical calculations used to demonstrate its validity. Then, we use this method to investigate several potential *Lg*-wave excitation mechanisms involving scattering. In section 4, by using 2D finite-difference simulation in the near source region, we investigate the contribution from near source volumetric scattering. In section 5, with a 2D boundary element method, we investigate the contribution from the rough topography. In section 6, we use a 3D finite-difference method to investigate the contribution from 3D scattering, including both volumetric and surface effects.

3. METHODOLOGY

3.1. The Near-Source Strategy

We limit our detailed near-source simulation to a relatively small model and analyze the wavefield within the model to investigate the source energy partitioning and the excitation of trapped regional phases such as Lg . The numerical methods used for this purpose should be capable of handling complex velocity models, e.g., volume heterogeneities and rough free-surface, and different types of sources. Here we use the full-wave finite-difference or finite-element methods for 2D calculation and use a finite-difference method with rough topography capability for 3D simulation. Many authors (e.g. Frankel, 1989; Xie and Lay, 1994; Vogtjard, 1997) have pointed out that for S-wave energy to be trapped in the waveguide, reverberating to generate the Lg -wave, it must propagate with post critical angle at the Moho discontinuity. However, in the waveguide and especially in the near-source region, the wavefield is highly complex. It is impractical to trace each phase in the space-time domain. An alternate, but equally valid way of tracking the wave energy is in the slowness domain. Multiply-reflected waves may arrive simultaneously in time, but in the slowness domain their energy distribution gives clear information about the wave intensity, slowness, and propagation direction. Several methods can be used to transfer space-time domain data into slowness (or equivalently wavenumber) domain information, for example, FK analysis or slant stacking. Here we employ a time-domain local slant stacking method (Xie and Lay, 1994; Xie et al. 2005a) to conduct slowness analysis, working simultaneously in both the space and slowness domains. The method has two major advantages. First, it allows analysis of the near-source processes in multiple domains, including space, time, slowness and frequency. This allows isolation of different excitation and partitioning mechanisms within the complex near-source environment. Second, the embedded array slowness analysis method can be applied at a close range, well before the Lg -wave is actually formed. This allows numerous simulations for a relatively small scale velocity model with very fine near-source structures. Since this is a computationally efficient approach, we can investigate energy partitioning mechanisms over a broad frequency range and a large source/model parameter space. For models with random structural features, multiple realizations (hundreds) are calculated and the results are treated statistically.

3.2. Local Slowness Analysis

Since the time-domain wavefield does not directly provide the propagation direction, we can decompose the wavefield into vector slowness domain using a local slant stacking method (Xie and Lay, 1994; Xie et al., 2005a)

$$\mathbf{u}(\mathbf{r}, \mathbf{p}, t, \omega) = \frac{1}{C_1} \sum_{\mathbf{r}'} W_R(\mathbf{r}' - \mathbf{r}) \mathbf{u}[\mathbf{r}', t - \mathbf{p} \cdot (\mathbf{r}' - \mathbf{r}), \omega], \quad (1)$$

where \mathbf{r} is the 3D position vector, \mathbf{r}' is the location of the receiver, t is time, $\mathbf{u}(\mathbf{r}, t, \omega)$ is the bandpass filtered synthetic seismogram with central frequency ω , $W_R(\mathbf{r}' - \mathbf{r})$ is a space window centered at \mathbf{r} , $\mathbf{p} = p\hat{\mathbf{e}}_p$ is the slowness vector, $\hat{\mathbf{e}}_p$ is the unit vector of the slowness

direction, $p = v^{-1}$ is the wave slowness, $v = v_p$ or $v = v_s$ is P - or S -wave velocity, C_1 is a normalization factor determined by the size of the space window and bandwidth of the frequency filter, etc. The space window is for a small seismic array with size related to both space resolution and slowness resolution. A larger array gives better slowness resolution but tends to smear the spatial resolution, while a small array gives better spatial resolution but less accurate slowness calculation. A proper trade-off between space and slowness resolution is required. The receiver interval should be small enough to avoid spatial aliasing. The average energy density of the wavefield as a function of space, time, slowness and frequency can be obtained as

$$D(\mathbf{r}, \mathbf{p}, t, \omega) = \rho \bar{u}^2(\mathbf{r}, \mathbf{p}, t, \omega), \quad (2)$$

and the energy flux related to slowness vector \mathbf{p} can be calculated as

$$\mathbf{J} = v D(\mathbf{r}, \mathbf{p}, t, \omega) \hat{\mathbf{e}}_p, \quad (3)$$

where ρ is the density and $\bar{u}(\mathbf{r}, \mathbf{p}, t, \omega)$ is the rms amplitude of the stacked velocity seismogram $\mathbf{u}(\mathbf{r}, \mathbf{p}, t, \omega)$. Similarly, we can slant stack seismograms according to their horizontal slowness \mathbf{p}_h

$$\mathbf{u}(\mathbf{r}, \mathbf{p}_h, t, \omega) = \frac{1}{C_2} \sum_{\mathbf{r}'_h} W_R(\mathbf{r}'_h - \mathbf{r}_h, z) \mathbf{u}[\mathbf{r}'_h, z, t - \mathbf{p}_h(\mathbf{r}'_h - \mathbf{r}_h), \omega], \quad (4)$$

where \mathbf{r}_h is the horizontal position and $\mathbf{r} = (\mathbf{r}_h, z)$, W_R is a 2-dimensional space window, and C_2 is a normalization factor similar to C_1 in equation (1). The average energy density as a function of \mathbf{p}_h can be expressed as

$$D(\mathbf{r}, \mathbf{p}_h, t, \omega) = \rho \bar{u}^2(\mathbf{r}, \mathbf{p}_h, t, \omega). \quad (5)$$

The pure horizontal energy flux related to horizontal slowness \mathbf{p}_h can be obtained from equation (3)

$$\mathbf{J}_h(\mathbf{r}, \mathbf{p}_h, t, \omega) = \int \mathbf{J}(\mathbf{r}, \mathbf{p}, t, \omega) \cdot \hat{\mathbf{e}}_h dp_z. \quad (6)$$

In the waveguide, the energy passing through a surface S within a frequency range Ω , a time window T and a slowness band P can be calculated as

$$E(S, P, T, \Omega) = \int_S \int_P \int_T \int_\Omega \mathbf{J} \cdot \hat{\mathbf{e}}_n d\omega dt d\mathbf{p} ds, \quad (7)$$

where $\hat{\mathbf{e}}_n$ is the unit normal vector of the surface element ds , and $d\mathbf{p} = dp_x dp_y dp_z$. When choosing a vertical intersection as the surface, equation (7) becomes

$$E(S, P, T, \Omega) = \int_S \int_P \int_T \int_\Omega J_h d\omega dt dp_x dz. \quad (8)$$

Equations (7) and (8) provide the basis for extracting energy from joint domains. To investigate the near-source energy partitioning and regional phase excitation, the energy generated from specific mechanisms is decomposed into multiple domains and analyzed based on its dynamic and kinematic properties. The condition for energy to be trapped in the crustal waveguide, i.e., $|\mathbf{p}_h| \geq 1/v_{S-\text{mantle}}$ (where $v_{S-\text{mantle}}$ is the upper mantle S velocity) is applied. We then use the joint window (S, P, T, Ω) to sort the trapped energy and estimate the contribution of specific mechanisms to regional phases such as Lg . Equations (7) or (8) can be partially integrated, which allows the energy to be projected onto different domains. The analysis within multiple domains provides additional information to characterize the contributions from different mechanisms. This method has the flexibility that we can either intercept the entire waveguide energy flux or just monitor the energy from specific phases or mechanisms. The calculation using three-

dimensional slowness analysis has the advantage that energy is fully expanded in the entire slowness domain. The slowness vector \mathbf{p} for both P - and S -waves can be obtained independently, giving us more information to investigate complicated near-source processes. The calculation based on horizontal slowness analysis gives the energy as a function of horizontal slowness \mathbf{p}_h . It provides the necessary information to separate the trapped and leaking energy. Although it does not directly give the full slowness domain information, by combining dynamic and kinematic characteristics, we can resolve the near-source phenomena in most cases without ambiguity.

Equations (7) and (8) are expressed with energy, since energy can be directly summed. However, regional phase observations are usually taken from amplitudes. To compare the numerical prediction with observations, we calculate the normalized square root of the energy

$$A = (E / E_0)^{1/2}, \quad (9)$$

where E_0 is a normalization factor which can be seen as the response from a unit source that has the same source time function as that used in the simulation. Normalized square root energy A is consistent with the conventional Lg -wave measurement based on the rms amplitude of the waveforms. Another advantage of using A is that the variation of amplitude distribution is smoother than the variation of energy. For these reasons, throughout this report, we will use the normalized square root energy in all figures although we sometimes simply call it “energy”.

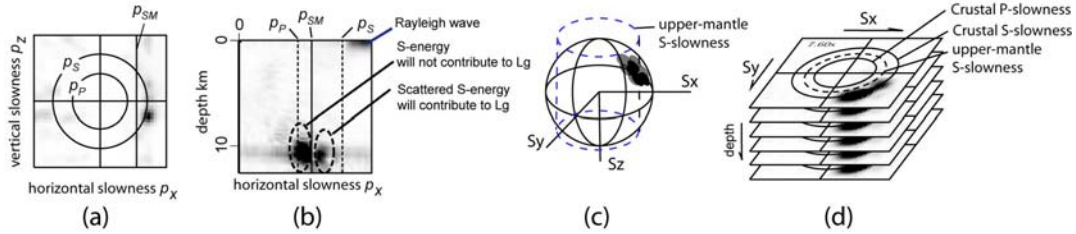


Figure 1. Different slowness domain displays for 2D and 3D models. For 2D model: (a) energy distribution as a function of slowness \mathbf{p} , and (b) as a function of horizontal slowness p_h and depth z . For 3D model: (c) energy distribution as a function of slowness \mathbf{p} and (d) as a function of horizontal slowness \mathbf{p}_h and depth. Energy with horizontal slowness larger than the upper mantle S-wave slowness will be trapped in the waveguide and will form guided S phases like Lg .

The above equations are for 3D models. In a 2D model, the y -component disappears and there is only x and z components left. Figure 1 shows different energy distributions in slowness domains for 2D and 3D models. Depending on the purpose, the energy can either be expressed as a function in slowness domain, or as a function in mixed slowness-depth domain. The upper mantle S-wave slowness $1/v_{S-mantle}$ is marked for different cases. All S -wave energy with horizontal slowness larger than the upper mantle S -slowness, whether directly radiated from the source or generated as secondary phases, will be trapped in the crustal waveguide and will contribute to the guided regional phases unless subsequent scattering causes it to leak out. Figure 2 is a sketch showing the

configuration of the local slowness analysis method for investigating the near-source processes. The model uses an explosion source, a fine scale near-source velocity model and a short distance receiver array to provide synthetic seismograms for the ensuing slowness analysis.

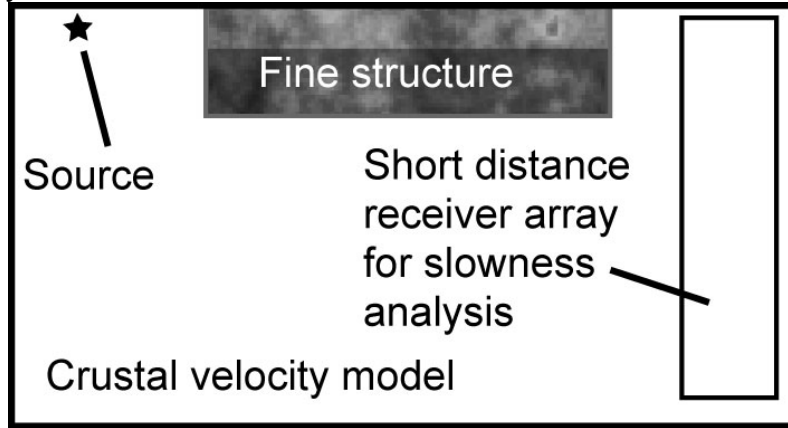


Figure 2. Configuration of the model for investigating near-source processes.

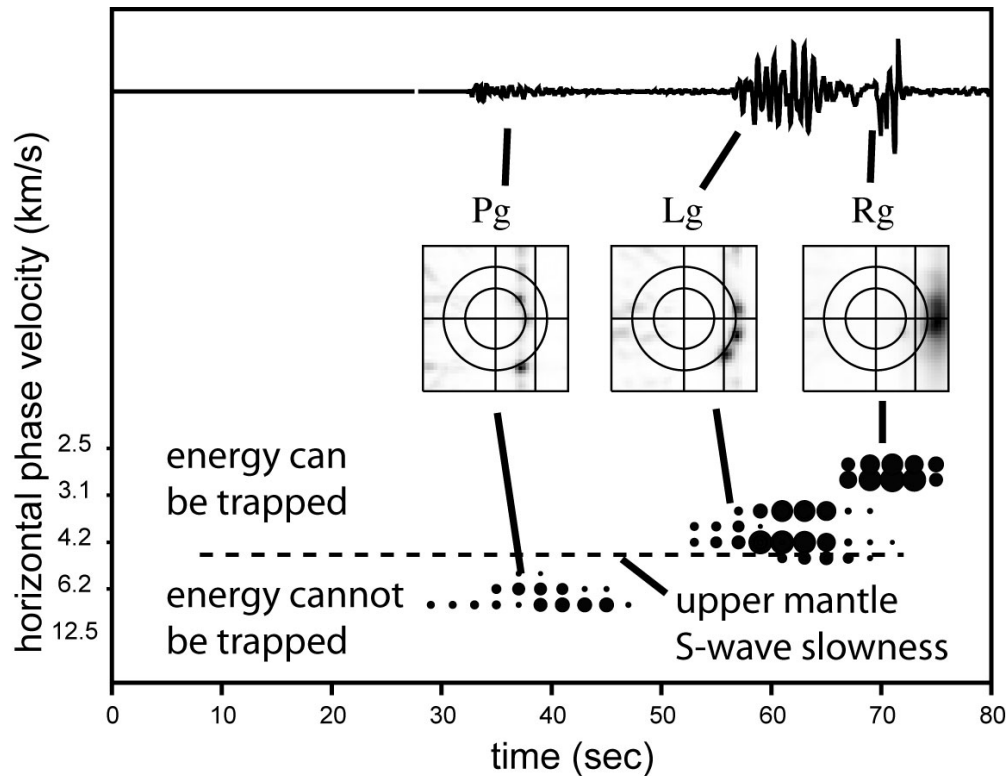


Figure 3. Example of slowness analysis at 180 km distance.

Figure 3 gives an example of slowness analysis. Shown on the top is the synthetic seismogram at the center of the mini array. In the middle are energy distributions for P -coda, Lg and Rg -waves in 2D slowness domain. These energy distributions clearly show that the P -coda is composed of P - and reflected pS -waves. Both of these have relatively

small horizontal slowness. The *Lg*-wave is composed of multiply reflected *S*-waves. Its energy falls on the *S*-wave slowness circle, and part of the energy stays on the right of the upper mantle *S*-slowness and forms trapped phases. The *Rg*-wave is also a trapped mode with horizontal slowness larger than the *S*-slowness. Shown at the bottom of Figure 3 is the energy isolated by the slowness analysis. The horizontal axis is time or, equivalently, the inverse of the group velocity. The vertical coordinate is the horizontal slowness or, equivalently, the apparent horizontal phase velocity. The solid circles are energy measured in the slowness domain with their sizes being proportional to the amount of energy. The horizontal dashed line marks the upper mantle *S*-slowness that divides the trapped and leaky energy.

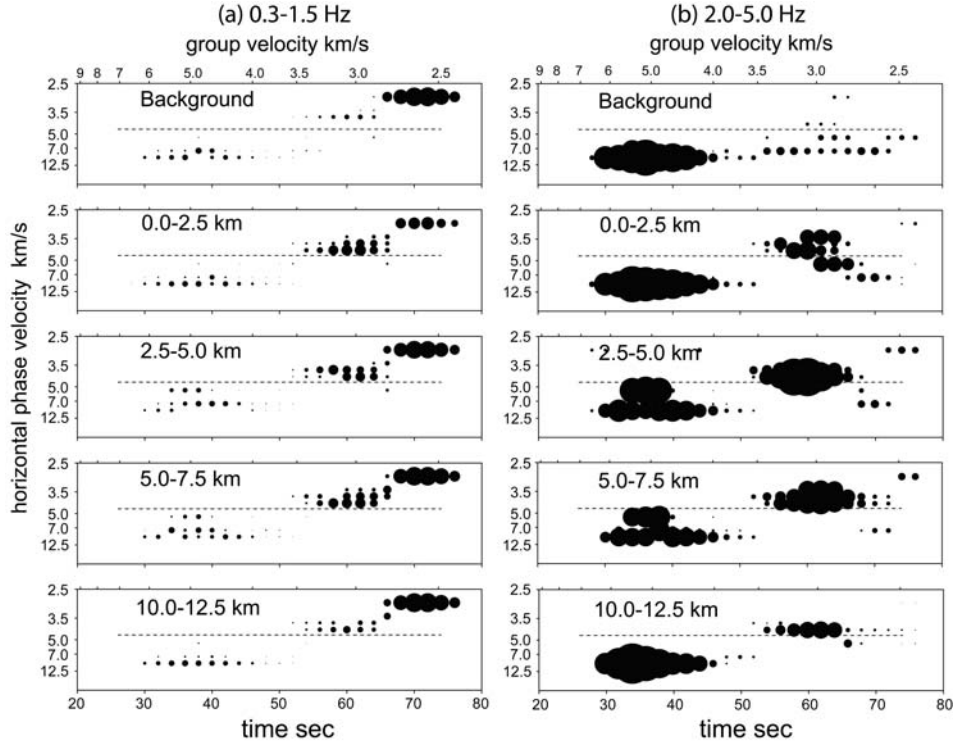


Figure 4. Slowness analysis calculated for the EK model and EK model with random patches at different depths. Column (a) is for frequency band 0.3-1.5 Hz, (b) is for 2.0-5.0 Hz. The top row is for background velocity model and the lower rows are for models with random patches. The depths of random patches are labeled in the panels. Details see the text.

3.3. The Energy Partitioning Formalism

For convenience, we symbolically write the near-source energy partitioning process for an explosion source as

$$E^K(p, f) = S(f)R^K(p, f), \quad (10)$$

where $E^K(p, f)$ is the near-source energy partitioned to the type K wave (K can be P , S , Lg , Rg or other wave types), p is the slowness, f is the frequency, $S(f)$ is the spectrum

of an isotropic explosion source. $R^K(p, f)$ is the energy response function of the near source structure for exciting type K wave, and can be expressed as

$$R^K(p, f) = R_F^K(p, f) + \sum_J R_F^J(p, f) T^{J \rightarrow K}(p, f) - \sum_J R_F^K(p, f) T^{K \rightarrow J}(p, f). \quad (11)$$

On the right hand side of this equation, $R_F^K(p, f)$ is the response of a flat, homogeneous layered earth model, partitioning the source energy into different phases. The transfer function $T^{J \rightarrow K}$ provides the J -to- K coupling which modifies the original partitioning by moving energy from one phase to another. The second term on the right hand side denotes energy being imparted into the K wave through coupling and the third term denotes energy lost from the K wave to other phases. The combined effect gives the total partitioning of the energy radiated from an isotropic source into the K wave energy distributed in slowness and frequency domains. This energy will develop into different regional phases which propagate to remote distances. Having a complete description of the slowness distribution allows us to accurately predict energy imparted to the distant regional phases based on the near-source energy budget.

Table 1. Eastern Kazakh Model

top of layer (km)	V_P (km/s)	V_S (km/s)	ρ (gram/cm ³)
0.0	5.05	2.91	2.70
1.0	5.66	3.21	2.70
5.0	5.55	3.17	2.70
10.0	6.01	3.41	2.70
15.0	6.29	3.55	2.90
25.0	6.65	3.73	2.90
30.0	6.89	3.85	2.90
45.0	7.59	4.20	3.00
47.5	8.33	4.57	3.30

Investigating these response and transfer functions provides a way to estimate the underlying process of energy partitioning. Due to the diverse mechanisms involved, the actual near-source energy partitioning can be highly complex. Factors such as the source depth, local layered structure, attenuation, random volumetric velocity perturbations and free surface fluctuations all affect the partitioning. These effects often contribute to the partitioning in a coupled way and the entire process is not necessarily linear or simply separable. In this study, we focus on the contribution from surface scattering. We use accurate numerical modeling to simulate the complex partitioning process and the slowness analysis to calculate the discrete response functions. The above symbolic equations provide us with a basic formalism for understanding the process. The embedded array method cannot characterize all partitioning coefficients, but is particularly well suited to characterizing relative changes in the trapped energy distribution for waves that will travel to large distances in the crustal waveguide.

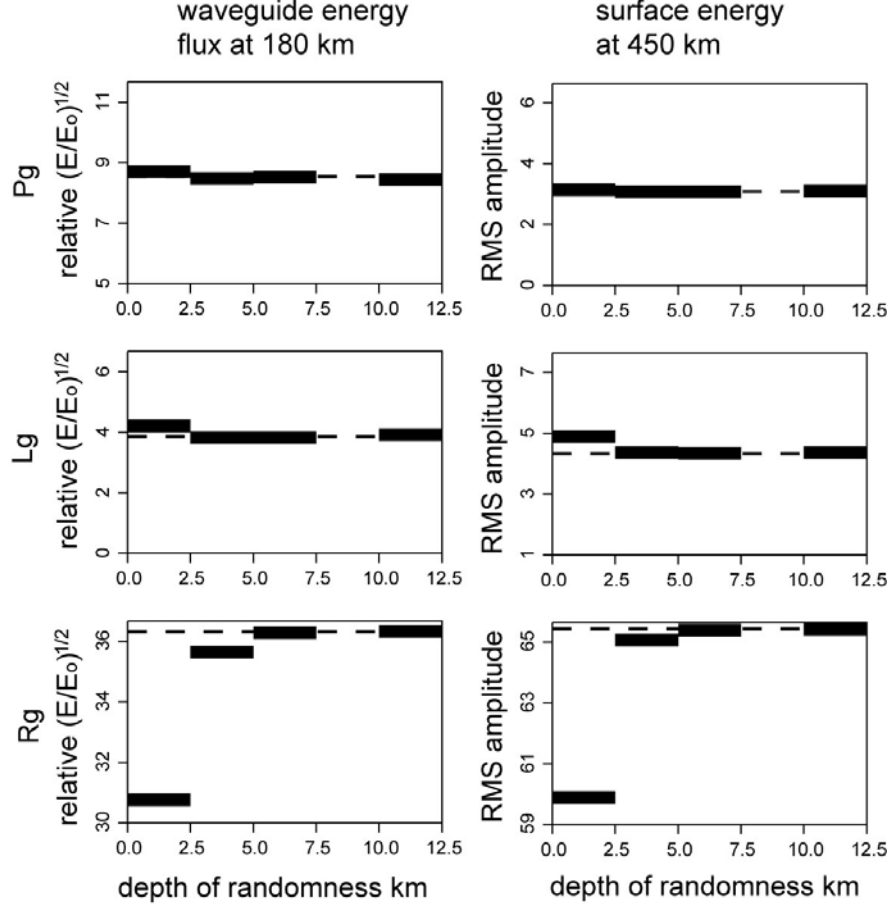


Figure 5. Comparison between waveguide energy flux at 180 km (left column) and the wave energy on the surface at 450 km (right column) for Pg, Lg and Rg windows. The frequency range is 0.3-1.2 Hz. Shown in each panel is relative energy versus the depth of random patches. Dashed lines indicate the energy level for background model and short bars indicate the energy changes due to the near-source scattering. If the FDSA method works, the two columns should be consistent.

3.4. Testing the Validity of the Method

We will first check the validity of the FDSA method by comparing the energy partitioning predicted at short distances using slowness analysis with the energy measured from long distance surface receivers using a conventional method. For all numerical examples calculated in this paper, unless otherwise indicated, we use the horizontally layered Eastern Kazakh (EK) model (Priestley et al., 1988) as the background and modify it by adding random velocity fluctuations at different locations. The EK model (Table 1) has a high velocity top layer with $v_p = 5.05$ km/s and an upper mantle S -wave velocity $v_{S-mantle} = 4.57$ km/s. For this layered model, P -waves radiated from an explosive source cannot be effectively converted to trapped S -waves. The random velocity perturbations added have an exponential power spectrum with horizontal and vertical correlation lengths equal to 0.5 km. We call the part of the model with

velocity perturbations the “random patch”. Within the patch, both P - and S -wave velocities have the same relative rms perturbation and the relative density perturbation is 50% of the relative velocity perturbation. To eliminate the possible effect of sharp edges of these random patches, a space window with smoothed edges is applied to the patch. The sizes, locations and the rms perturbations of these patches will vary depending on the purpose of the investigation.

We first test models with scattering at different depths by varying the location of random patches within the EK model. These patches are 2.5 km in vertical extent, extend horizontally from 5 to 25 km and are located at different depths. Within the patches, the P - and S -wave velocities have 10% rms fluctuations. An explosion source is located at depth 0.5 km. Figure 4 shows the slowness analysis results at a distance of 180 km in the crustal waveguide. Columns (a) and (b) are for frequencies 0.3-1.5 Hz and 2.0-5.0 Hz, respectively. Each panel is similar to the example shown in Figure 3. The top row is for the background velocity model and the other rows are calculated for models with near-source random velocity perturbations. The depths of the random patches are labeled in the figure. We first focus on the low-frequency results in column (a). For the background velocity model, there is a strong Rg phase but very little energy within the Lg group velocity window of 3.0-3.5 km/s, which is typical for a crustal model with a high velocity top layer. For models with random velocity patches, compared with the background model, considerable energy is transferred to the Lg -wave through scattering, while the Rg -wave is weakened. The tendency is that the shallower the random patch, the more energy is scattered into Lg . For the EK model, which has a thick high speed crust, the distance for Pn to cross Pg at the free surface is about 200 km. At 180 km distance, there is no prominent Pn energy shown in this analysis.

For high frequency results in column (b), from the top panel we see strong Pg energy. There is also energy within the Lg group velocity window. However, this energy has a similar horizontal slowness to the Pg -wave, implying that it is generated from Pg through P -to- P and P -to- S reflections on the free surface and interfaces such as the Moho discontinuity. Although the energy exists at short distances, the steep incident angle causes energy to gradually leak to the upper mantle through multiple reflections and it cannot form trapped regional phases. In the other panels, after adding random velocity perturbations in the near-source region, part of the P energy transfers to the Lg wave, i.e., energy falls into the proper group velocity and slowness windows. In general, the scattering affects Rg -to- Lg energy at low frequencies and affects P -to- Lg coupling at high frequencies. Summing up energy through the waveguide cross section and within the proper time (group velocity) windows allows the energy for the related wave types to be obtained. Specifically, summing up the energy located within the Lg group velocity window and above the upper mantle S -slowness allows Lg energy at long distances to be predicted. It is necessary to confirm this calculation.

Figure 5 compares the waveguide energy obtained using different methods. The left panel shows the square root energy passing through the waveguide cross section at 180 km calculated from the slowness analysis shown in Figure 4 and the right panel shows the rms amplitudes at 450 km calculated using a conventional processing

technique (i.e., computing surface synthetic seismograms, applying frequency filters and group velocity windows to isolate different phases, and calculating rms amplitudes for these phases.). The same velocity model used in Figure 4 is adopted here and a full-scale finite-difference simulation is computed to provide data up to 500 km distance. For simplicity, we label the predicted trapped energy as “Lg” energy. The relative energy changes of Pg-, Lg- and Rg-waves, as functions of the depth of the random velocity patches are shown in Figure 5. The calculations for different phases demonstrate that the relative change of energy obtained in the waveguide slowness analysis corresponds closely to that obtained on the free surface, even for dramatic changes such as the strong scattering of Rg. The results confirm that the slowness analysis within the waveguide correctly predicts the surface regional observations at greater distance.

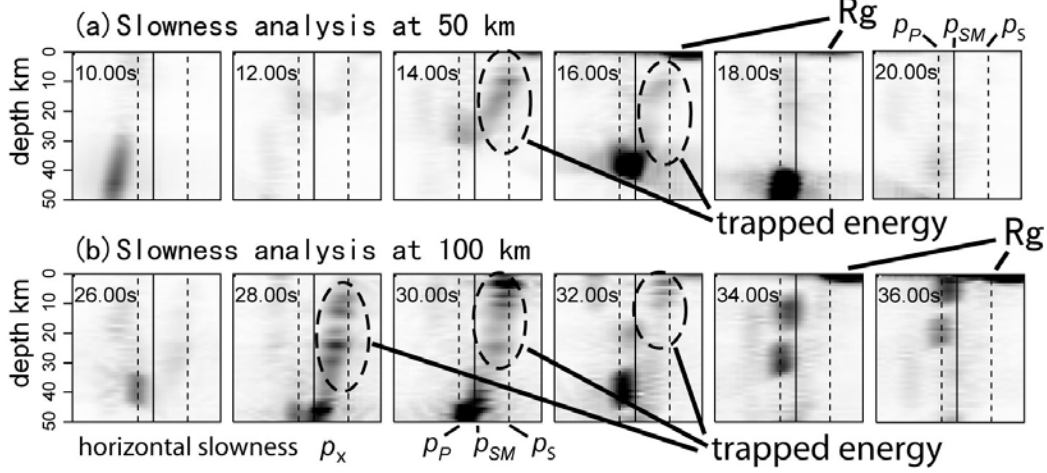


Figure 6. Examples showing the slowness analyses at distances (a) 50 km and (b) 100 km.

The p_{SM} , p_P and p_S are upper-mantle S-slowness, crustal P-slowness and S-slowness, respectively. The energy that can be trapped in the crustal waveguide is indicated in the figure.

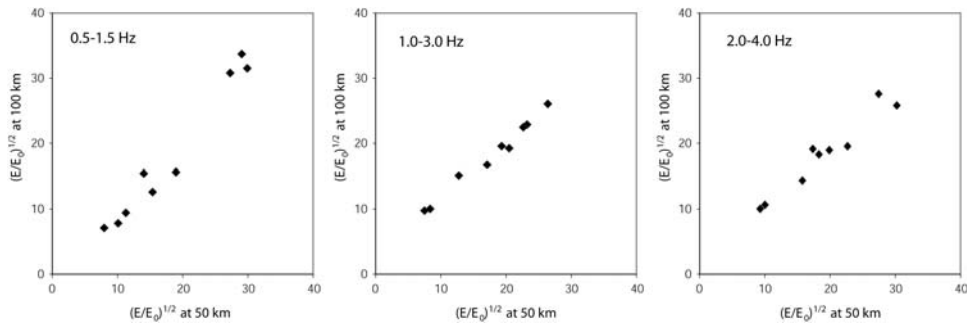


Figure 7. Comparison between trapped waveguide energy measured at 50 km (horizontal coordinate) and 100 km (vertical coordinate) for frequency bands 0.5-1.5 Hz, 1.0-3.0 Hz and 2.0-4.0 Hz. Different dots are results from different velocity models and source depths. The results show a general linear relationship for all frequencies.

To examine the energy flux measurements obtained at even shorter distances, we compare the slowness analysis measurements at 50 km with those at 100 km. For these two distances, Figure 6 gives examples of horizontal slowness analyses, which show quite different features in the slowness-depth domain due to evolution of the wavefield with range. Figure 7 compares the corresponding waveguide energy measured at these two distances for different frequency bands. The vertical and horizontal coordinates are for measurements at the two distances and dots represent results for different source depths and velocity models. Although a wide range of near-source structures and source depths are used to generate these measurements, the results show a general linear relationship for all frequency bands. This further verifies that we can use a small model to investigate the near-source energy partitioning robustly.

4. Regional Phase Excitation: Contributions from Volumetric Scattering

To investigate scattering contributions from volumetric heterogeneities, we use a 2D finite-difference method to simulate the wave propagation. The model uses an explosion source, a fine scale near-source velocity model and a short distance receiver array to provide synthetic seismograms for the ensuing slowness analysis (see Figure 2).

4.1. *P*-*pS*-to-*Lg* and *P*-to-*Lg* Conversion

We first investigate the *P*-*pS*-to-*Lg* conversion caused by near-source lateral velocity variations and assess its effect on the explosion *S*-wave energy budget. In a horizontally layered model with overburden *P*-wave velocity larger than the upper mantle *S*-wave velocity, the free surface reflected *pS*-wave has a steep incidence angle and cannot be trapped in the crustal waveguide to form *Lg*. In this case, the energy transfer through *P*-*pS*-to-*Lg* coupling is almost zero. Although it is generally agreed that the existence of near-source lateral velocity variation can increase the *P*-to-*Lg* energy exchange, the detailed mechanism underlying this process is still not fully understood.

Figure 8 compares the simulated *P*-*pS*-to-*Lg* coupling in models with and without near surface lateral velocity variations. Figure 8a is for the EK-model. A shallow explosion source located at depth 0.5 km generates *P*, *pS* and *Rg* waves. Two-dimensional slowness analysis is conducted for selected phases in the wavefield and the results are shown together with the wavefield snapshot. The synthetic seismograms were bandpass filtered between 2.0 and 6.0 Hz before the slowness analysis. As can be seen from the result, the *P*-wave leads the wavefield and has a distinct slowness. Reverberations within the uppermost crust causes multiply parallel *pS* wavefronts with their horizontal slowness approximately equal to the overburden *P*-slowness. The *pS* energy stays to the left of the upper-mantle *S*-slowness and there is no energy transferred from *P* to *Lg*. In Figure 8b, a shallow random velocity patch is added to the EK-model to test the effect of near surface scattering. The random patch has a 5% rms velocity fluctuation and is located at distances 5 to 15 km and depths 0 to 2.5 km (shown in the snapshot as a shaded area). The slowness analyses are conducted for *P*, *pS* and *pS*-coda. Although *P*- and early *pS*-waves are barely affected, the *pS*-coda clearly contains some scattered energy with horizontal slowness to the right of the upper-mantle *S*-slowness.

To investigate further the scattering from a shallow random patch, horizontal slowness analysis is conducted at a distance of 20 km and depth 0-12.5 km. Figure 9 shows the energy distribution in the slowness-depth domain with arrival times and major phases labeled in the frames. The two prominent down-going phases are the P -wave and the free-surface reflected pS -wave. The Rg energy enters the array at 6.0 s with its depth close to the surface and slowness beyond the S -slowness. Shown in row (a) is the result using the EK-model. Due to the nearly horizontal propagation of the P -wave at the free surface, the pS -wave energy has a horizontal slowness which is similar to the overburden P -slowness and the energy falls to the left of the upper mantle S -slowness. In rows (b) and (c), shallow random velocity patches with rms velocity fluctuations 3% and 5% are added to the EK-model at distances 5 to 15 km and depths 0 to 2.5 km (the same position as in Figure 8b). As can be seen in the figure, scattering causes part of the pS energy to cross the upper mantle S -slowness and build up in the dashed rectangles. At shallow depths, the slowness of the scattered energy approaches the S -slowness. With an increase in depth, the slowness of this energy gradually merges with the P -slowness. The slowness behavior is consistent with scattering of waves at shallow depths, increasing as shallow heterogeneity increases.

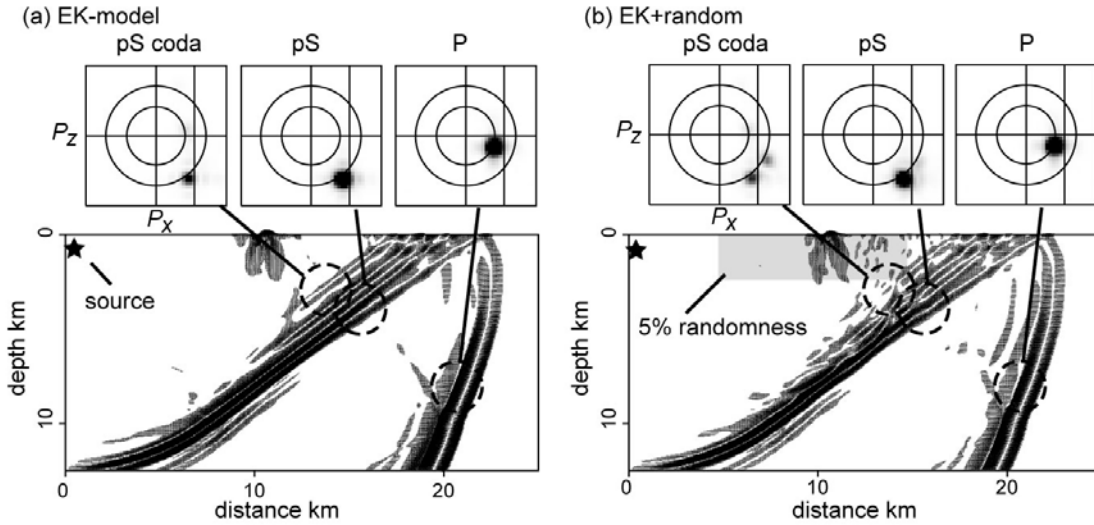


Figure 8. P-pS-Lg conversion due to shallow scattering. (a) is for the EK-model and (b) is for the EK-model with a shallow random patch. The random patch has a 5% rms velocity fluctuation and is shown as a shaded area between horizontal distances 5 to 15 km and depths 0 to 2.5 km. The snapshots and results of slowness analyses of P , pS and pS -coda are shown in the figure. Details are given in the text.

Figure 10 investigates scattering taking place at deeper depths. The configuration of the source and model is similar to that used in Figure 8b, except the random patch with 3% rms velocity fluctuation is added to the EK-model between distances 5 and 15 km and depths 2.5 and 10 km (shown in the snapshot as a shaded area). The 2D slowness analysis is conducted for selected phases in the wavefield and the results are presented in the figure. After passing through the random region, there is P -coda composed of scattered P - and S -waves generated from the direct P -wave. Although the early part of the pS -wave does not contribute to the trapped energy, its later part contains energy

located to the right of the upper-mantle S -slowness which therefore will contribute to the trapped regional phases. Figure 11 gives the energy distribution in the slowness-depth domain for different models where row (a) is for the EK-model and rows (b) and (c) are for the EK-model with 3% and 5% rms fluctuations in a random patch like that used in Figure 10. The slowness analysis is conducted at a distance of 20 km and for depths between 0 and 12.5 km. As expected, with the EK-model no energy is seen beyond the upper mantle S -slowness, but after the lateral velocity variations are introduced, energy starts to build up to the right of the upper-mantle S -slowness. Two types of scattered energy can be found in the slowness-depth domain: weak but widely distributed S energy (indicated by the dashed ellipses) and scattered energy linked to the pS -wave (indicated by the dashed rectangles). Both types of energy satisfy the criterion $p_x \geq p_{S-mantle}$ and will contribute to the Lg -wave. The widely spread scattered S -wave is generated by the P -to- Lg coupling through volumetric scattering. The scattering process redistributes the angle spectrum of the original incident waves. Since there is no lateral heterogeneity at the top of the crust, scattered pS -waves are generated by the interaction between distorted incident P -waves and a smooth free surface.

Comparing Figure 11 to Figure 9, the scattered pS -wave generated from a deeper random patch appears later than that from a shallow random patch. Both volumetric scattering and scattering near the free-surface affect the general P -to- Lg conversion.

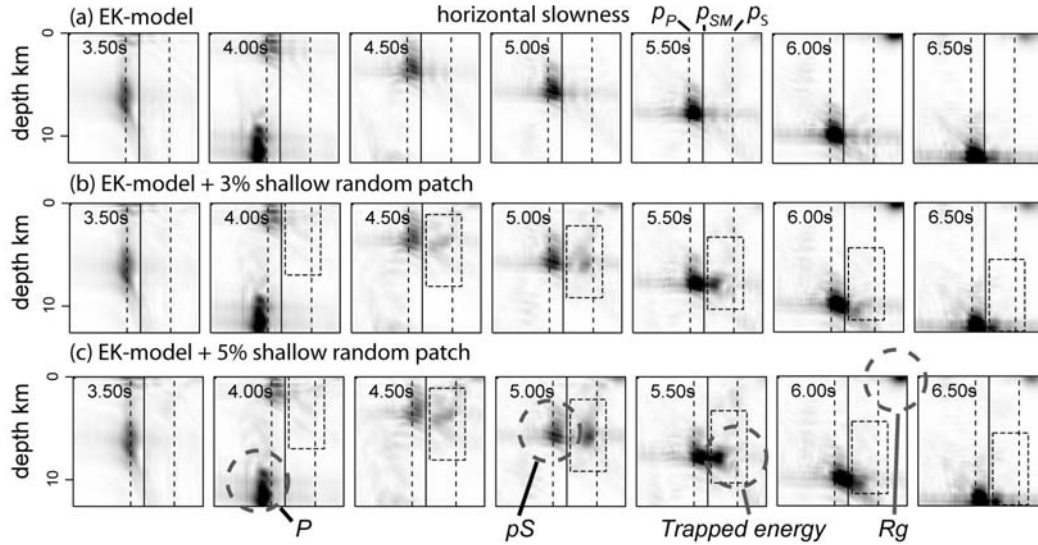


Figure 9. Horizontal slowness analyses for investigating the P - pS - Lg coupling with (a) the EK-model, (b) the EK-model plus a 3% shallow random patch and (c) the EK-model plus a 5% random patch. The slowness analyses are conducted at distance 20 km and for depth range 0 to 12.5 km. The configuration of the source and model is the same as that used in Figure 8. Major phases are labeled in the figure and energy circled by dashed rectangles is scattered pS -wave.

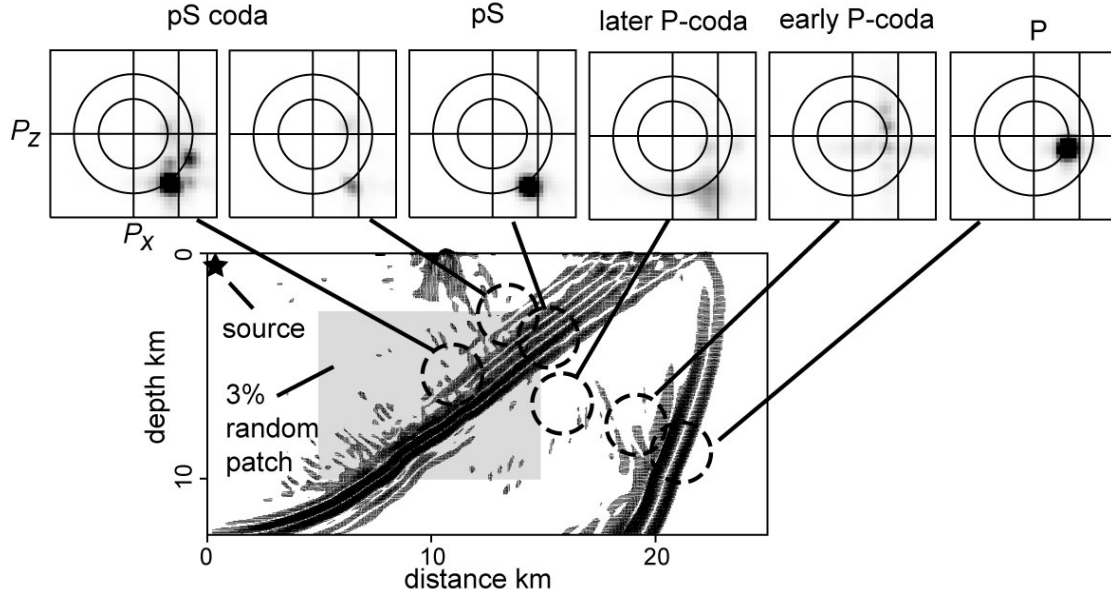


Figure 10. The P-pS-Lg conversion due to a deeper random patch. The random patch has a 3% rms velocity fluctuation and is shown as a shaded region between distances 5 and 15 km and depths 2.5 and 10 km. The slowness analysis for P, P-coda, pS and pS-coda are also shown in the figure.

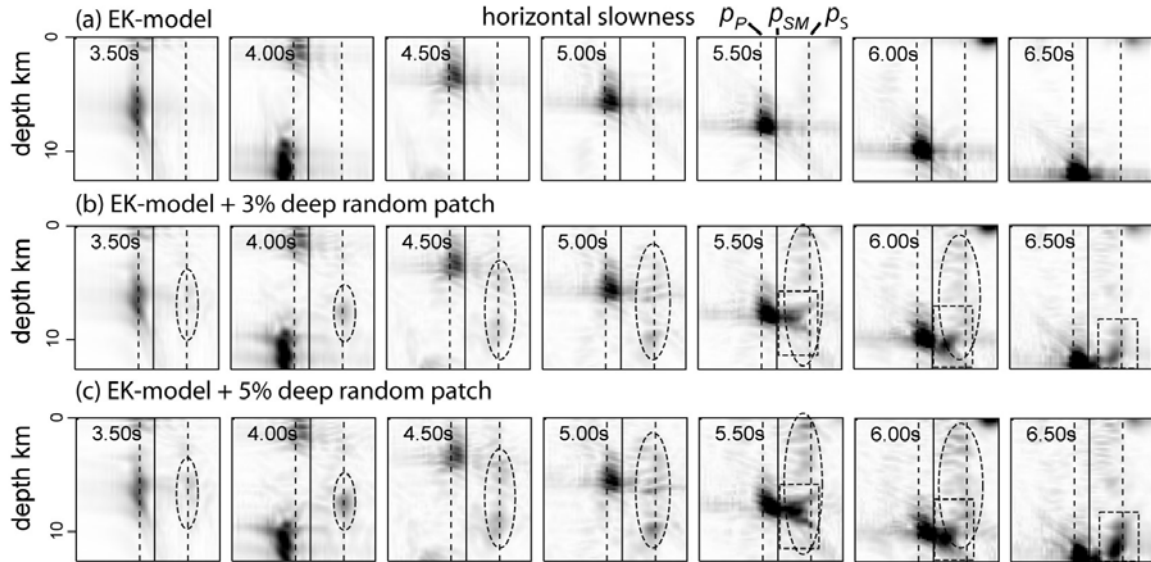


Figure 11. Energy distribution in depth and horizontal slowness domain for (a) the EK-model, (b) EK-model plus a 3% random patch and (c) EK-model plus a 5% random patch. The configuration of the source and model is same as that used in Figure 10. Energy circled by dashed rectangles is P-pS-Lg scattering and energy circled by dashed ellipses is P-Lg scattering.

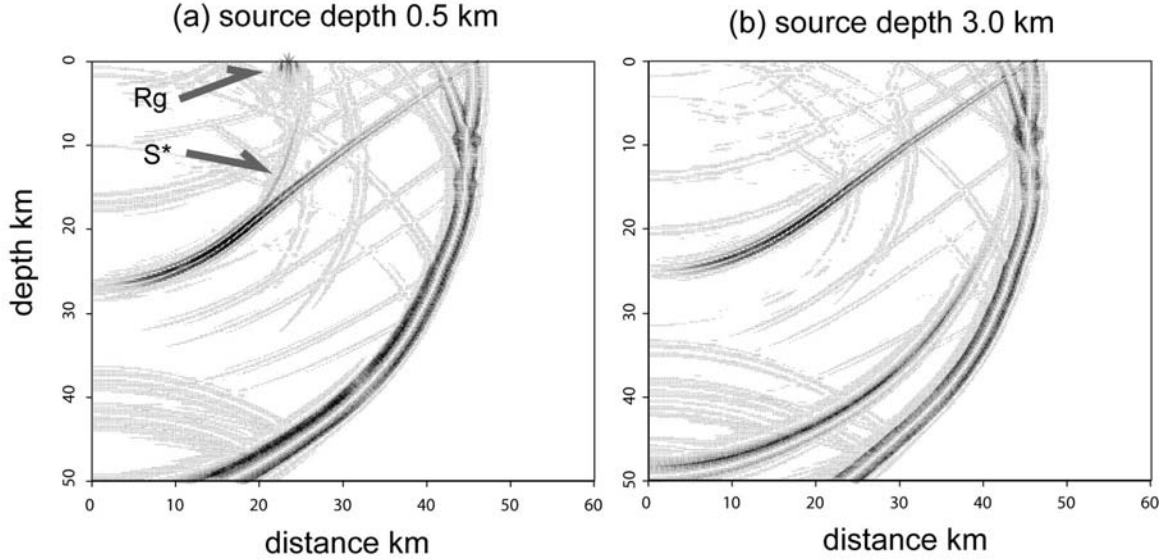


Figure 12. Wavefield snapshots for explosion sources at depths (a) 0.5 km and (b) 3.0 km. Note that a shallower explosion is a more

4.2. Contributions from the S^* -Wave

For shallow explosion sources, the S^* -wave may become a significant contributor to Lg (Gutowski, et al., 1984; Lilwall, 1988; Xie and Lay, 1994; Vogfjord, 1997). The amplitude of S^* can be large if the source depth is within a fraction of a wavelength from an interface. This makes its excitation highly dependent on the source depth and frequency. Figure 12 shows snapshots for explosion sources at 0.5 km and 3.0 km, respectively. The result clearly shows that a shallow source generates larger S^* - and Rg -waves. We investigate the contribution of the S^* -wave within the EK model. Figure 13 shows horizontal slowness analyses at a distance 35 km and for depths between 0 and 30 km. The time window is chosen between 11 to 13 s after the direct P -wave passes the receiver array. The synthetic seismograms are bandpass filtered between 1.0 - 5.0 Hz. The four rows from top to the bottom correspond to source depths 0.25 km, 0.5 km, 1.0 km, and 2.0 km, respectively. The major arrival is the down-going free surface reflected pS -wave, which has a horizontal slowness similar to the overburden P -slowness. As expected for a horizontally layered model, the pS energy stays to the left of the upper mantle S -slowness and has no contribution to the trapped regional phases. For shallow sources, the Rg -wave enters the array at about 12 s and its energy concentrates between 0 to 3 km, as can be seen on the upper right corners in the slowness-depth domain. For source depth of 2.0 km, the Rg -wave is very weak. The S^* -wave enters the array from a shallow depth and gradually merges with the pS -wave (also refer to Figure 12). The S^* -wave is strong for shallow sources and its amplitude decreases with increasing source depth. Very little S^* energy can be observed for source depths below 2 km. In the joint domains, the S^* -energy can be isolated and quantified even within a complicated wavefield, which is very difficult using remote surface synthetics. The dashed rectangles are the time-slowness-depth window used to locate the S^* energy. The time window is chosen after the arrival of direct P -wave, and a variable depth range is chosen to avoid

contamination from the Rg -wave. The slowness range is chosen between 0.23 and 0.34 s/km . The energy from successive windows can be summed together to give the contribution of S^* to the trapped regional phases.

efficient source for generating S^* and Rg -waves.

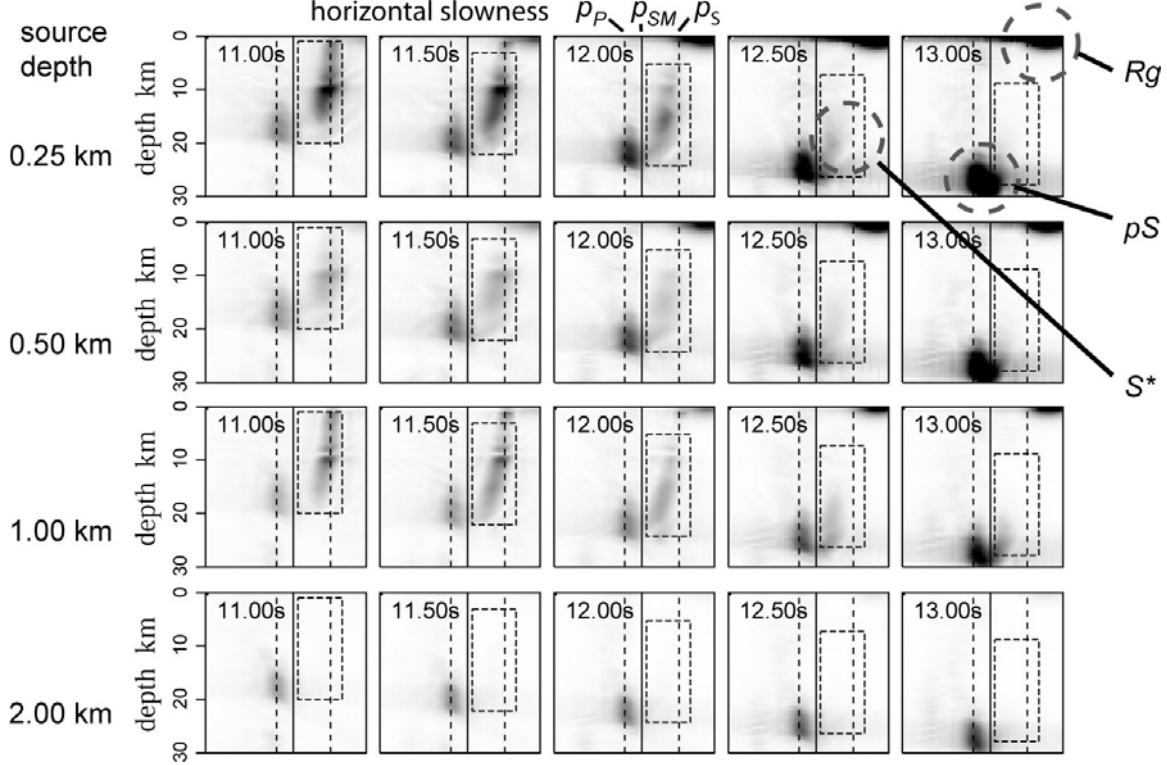


Figure 13. Slowness analysis for investigating S^* -to- Lg conversion. Different rows are for different source depths. Dashed rectangles indicate the time-space-slowness windows used to pick the S^* energy.

4.3. The Frequency Dependent Lg Excitation Function

The frequency dependence of Lg -wave excitation is rooted in the underlying physical processes and is usually controlled by different characteristic scales. For example, the excitation of Lg by S^* , Rg -to- S scattering and spall are all highly source depth dependent. The excitation spectra from individual or joint mechanisms contributing to regional phases depict the frequency dependence of these processes. Frequency dependent P/S ratios will depend on the excitation functions of multiple phases. We use FDSA to quantify Lg -wave excitation spectra from S^* - and pS -waves. Figure 14 gives the S^* -to- Lg excitation spectra as functions of source depth and frequency. The slowness analysis and multi-domain window used to pick the trapped energy are similar to that shown in Figure 13. A series of bandpass filters is used to give responses at different frequencies. The vertical coordinate is the normalized relative energy $(E/E_0)^{1/2}$. Since the source time function has been taken away, the excitation function is the impulse response

of the model to the source. The results clearly show that the S^* -to- Lg excitation is generally enhanced for lower frequency and shallow source depth. The major contribution comes from sources located above 1 km. For sources at depths below 1 km, only low frequency energy below 1 Hz has significant contribution to Lg -wave excitation. However, the responses are also model dependent. For a model with a homogeneous crust (Figure 14a), the distribution has simple monotonic tendencies in both source depth and frequency. For the EK model (Figure 14b), the excitation spectrum has a maximum at depth 1 km and a more complicated frequency dependence. This may reflect the fact that the EK model has an interface at 1 km depth. The S^* -waves generated or reflected from multiple interfaces may interfere with each other and give a complicated frequency spectrum.

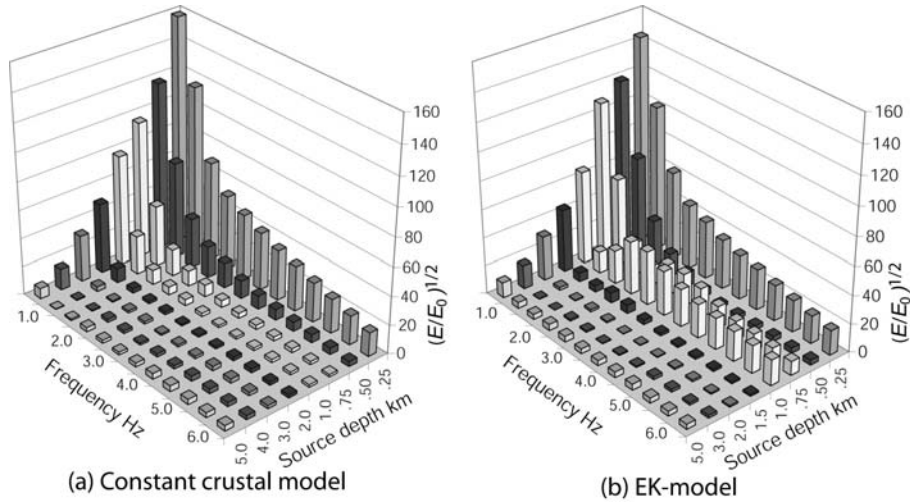
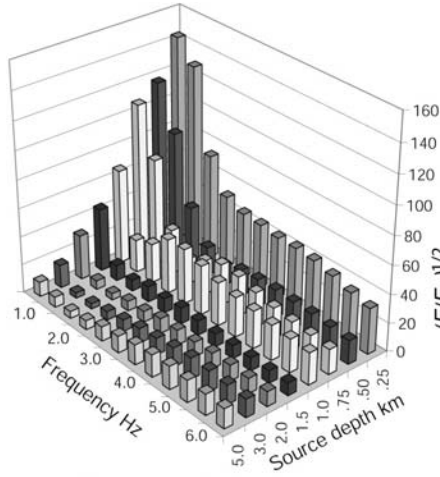
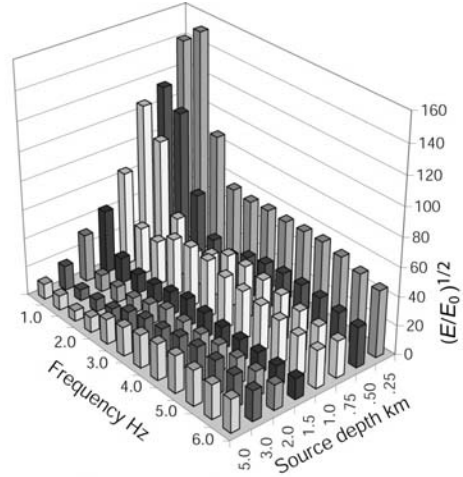


Figure 14. Normalized Lg excitation spectra for sources in different velocity models and at different depths with (a) a model with a homogeneous crust and (b) the EK-model.

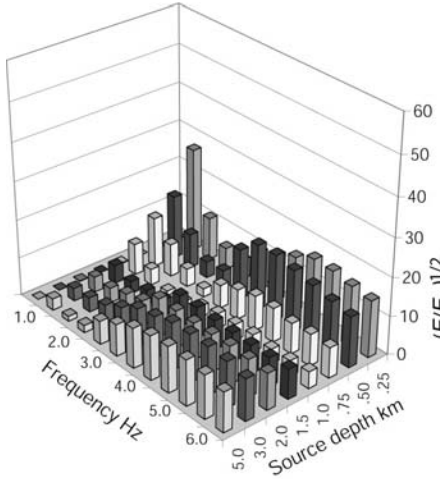
To investigate the combined effect for S^* -wave and near-source scattering, we add shallow random velocity patches to the EK model. The random patch extends between distances of 5 to 25 km and depths of 0 to 2.5 km. Shown in Figures 15a and b are excitation spectra for random patches with rms velocity fluctuations of 3% and 5%, respectively. The most prominent feature is the build up of high frequency energy. The scattered energy increases with rms velocity fluctuations. Figures 15c and d isolate the scattered energy by subtracting the excitation spectrum of the EK-model from the spectra for models with random velocity patches. Two types of energy can be identified within the frequency-depth domain. The high-frequency energy results from P - pS -to- Lg and P -to- Lg scattering. This energy is especially important for deeper sources to generate Lg -waves, since a deeper source generates little trapped energy in a horizontally layered model. The low-frequency energy concentrated at shallow source depths comes from Rg -to- Lg scattering.



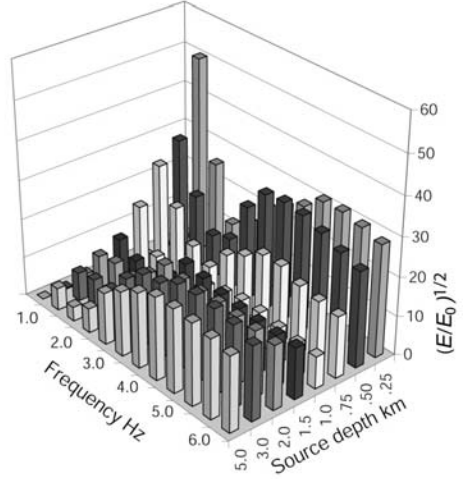
(a) EK+3% shallow random



(b) EK+5% shallow random



(c) EK+3% scattered energy



(d) EK+5% scattered energy

Figure 15. Normalized Lg excitation spectra for sources in the EK-model with shallow random patches, for (a) the EK-model with a 3% shallow random patch, (b) the EK-model with a 5% shallow random patch, (c) and (d) the isolated scattered energy in (a) and (b) respectively due to the random patches found by removing the energy for the layered models. Note different vertical scales are used for scattered energy.

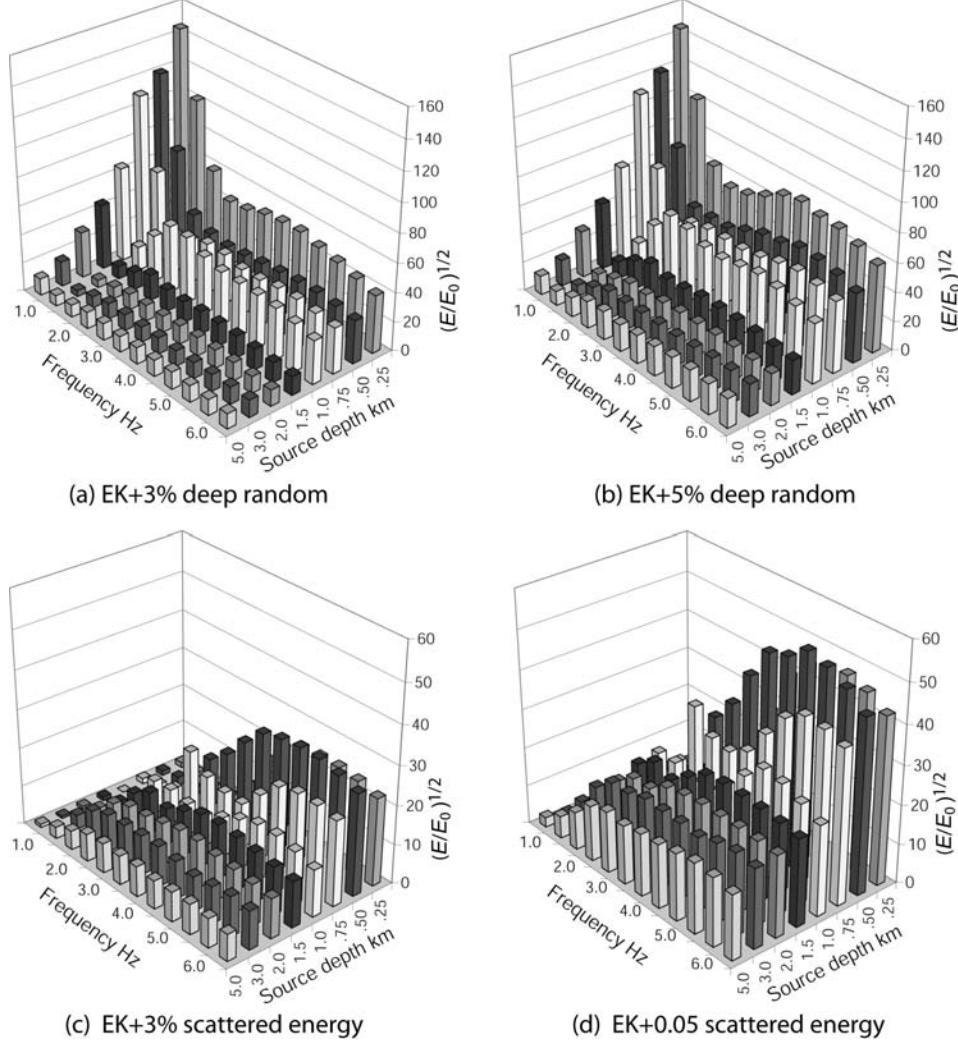


Figure 16. Normalized Lg excitation spectra for sources in the EK-model with deep random patches, for (a) the EK-model with a 3% deep random patch, (b) EK-model with a 5% deep random patch, (c) and (d) the isolated scattered energy in (a) and (b) due to the random patches.

Figure 16 gives the excitation spectra for the EK-model with deeper random patches. The random patch is located between distances 5 to 25 km and depths 7.5 to 10.0 km. Figures 16a and b give excitation spectra for random patches with rms velocity fluctuations of 3% and 5%, respectively. Figures 16c and d give the isolated scattered energy. The scattered energy from the deeper random patches has little low-frequency content, which supports the interpretation that the low-frequency energy comes from the *Rg*-to-*Lg* scattering. The frequency dependent excitation spectra establish the relationship between the observations and the characteristics of sources and near-source structures. They provide the basis for evaluating the dominant mechanisms for *Lg*-wave excitation.

5. Regional Phase Excitation: Contributions from Surface Scattering

Figure 17 shows the basic configuration of the calculation. Random topographic fluctuations described by an exponential power spectrum, a correlation distance and prescribed rms fluctuation are used for the free surface. We use a 2D P - SV wave boundary-element method (Ge et al., 2005) to generate synthetic seismograms for an isotropic explosion source. The boundary element method has been proven to be an accurate wave propagation approach when the earth model includes irregular surfaces. The synthetic seismograms are computed for an embedded vertical array of 41×90 receivers located between distances 30 and 50 km and depths 0 and 45 km (see Figure 1). The synthetic seismograms from the array are processed using the local slowness analysis method.

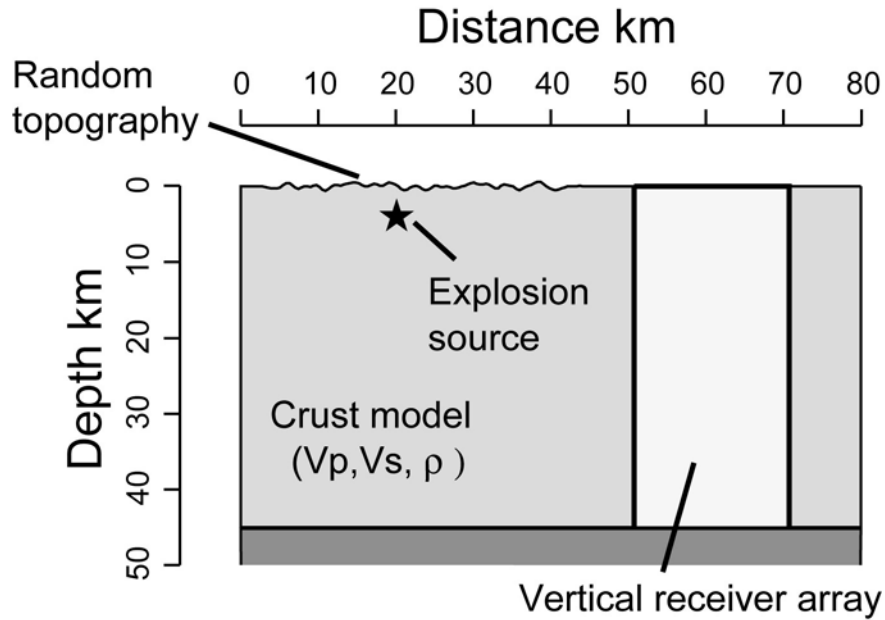


Figure 17. Configuration of the source, model and receiver array.

5. 1. Phenomena Resulting from Free Surface Scattering

Space domain representation of surface scattering

Illustrated in Figure 18 are boundary element generated snapshots for wavefields in a model with free surface scattering. The parameters of the three-layer velocity model are listed in Table 2. A random fluctuation with a correlation length of 0.5 km and a rms fluctuation of 0.15 km is used for the free surface and extends between distances 30 and 50 km. The source is located at distance 20 km and a depth of 0.5 km. Figures 18a and 18b are horizontal and vertical displacements. In addition to familiar major phases (e.g., P , pS , Rg) expected for a shallow explosion in a flat earth model, scattered body and surface waves from the rough free surface are present in the wavefield. The surface-to-body and body-to-body wave scattering is distributed through the entire medium

following the direct waves, and the body-to-surface and surface-to-surface wave scattering is concentrated at very shallow depths following direct waves as they graze the surface.

Table 2. Three-layer velocity model

Bottom of layer (km)	V_p (km/s)	V_s (km/s)	ρ (g/cm ³)
10	5.6	3.2	2.7
45	6.5	3.8	2.9
Infinity	8.0	4.5	3.3

Table 3. Two-layer velocity model

Bottom of layer (km)	V_p (km/s)	V_s (km/s)	ρ (g/cm ³)
45	6.5	3.6	2.9
infinity	8.0	4.5	3.3

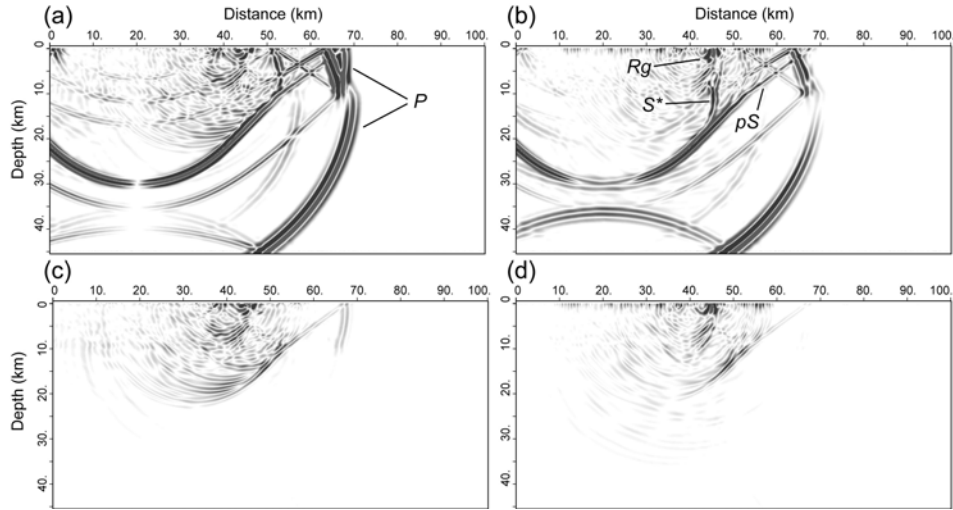


Figure 18. Wavefield snapshot at $t = 10.0$ s for a model with random free surface fluctuation, where (a) and (b) are horizontal and vertical components of the wavefield, and (c) and (d) are horizontal and vertical components of the scattered wavefield obtained by subtracting the flat model wavefield from the random surface wavefield. The source is at 20 km horizontal position and 0.5 km depth.

To isolate the scattered phases, we subtract the wavefield generated for a flat surface from the wavefield for the model having a rough surface, yielding the results presented in Figures 18c and 18d. Most of the scattered body waves are shear waves. Due to the coupling between different wavenumbers, the scattered body waves have a very broad range of propagation directions. The horizontal component includes mostly shear waves propagating with steep dip angles that will tend to contribute to teleseismic S -waves. The shear waves on the vertical component mostly have shallow angles and will contribute to crustal guided waves such as regional Lg . Although these space domain images are instructive for understanding some aspects of the surface scattering, to fully explore the

wave propagation characteristics in the complex near-source environment, we conduct slowness analysis for these wavefields. We note that any differences in wave excitation due to model variations relative to the reference flat surface case are captured in the differenced wavefields and may not be distinguishable from scattering effects, but statistical averaging over multiple model realizations does tend to isolate the scattering effects.

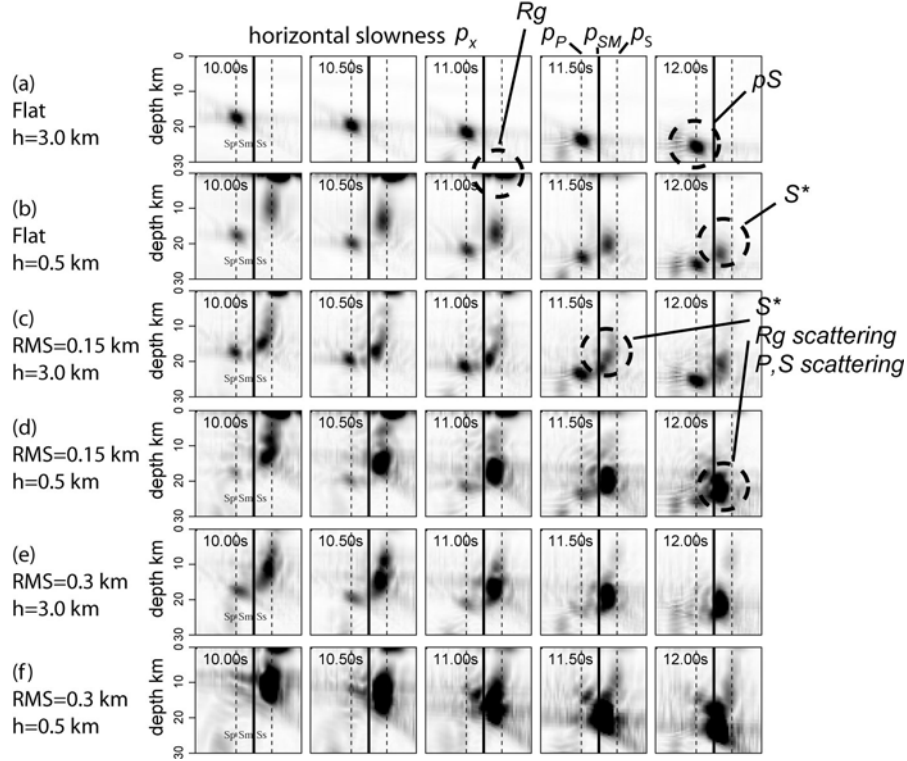


Figure 19. Slowness analysis results in the depth-slowness domain for discrete time intervals as the wave sweeps through the observing array for models with different source depths and free surface parameters. The frequency band is between 1.5 Hz and 4.5 Hz. All the panels are normalized in the same scale. In each small figure, the horizontal coordinate is horizontal slowness and the vertical coordinate is depth. The thick vertical line indicates the upper mantle S-wave slowness which separates energy that leaks out of the waveguide (to the left) from energy trapped in the wave guide (to the right) that forms Lg. The PP, PS and PSM are crustal P-wave, S-wave and upper mantle S-wave slownesses, with their values are 0.154, 0.28 and 0.22 s/km, respectively.

Slowness domain presentation of surface scattering

To quantify the scattered wavefield, we transform the signal to the slowness domain. We compute wavefields for the two-layer velocity model listed in Table 3. The random surface topographic fluctuation is located above the source and extends in both directions for 20 km. The random topography has an exponential power spectrum and its correlation distance, a , is 0.5 km. The rms fluctuations used are 0.15 km (maximum peak-to-trough 0.625 km) and 0.3 km (maximum peak-to-trough 1.281 km). Either a shallow source (depth = 0.5 km) or a deep source (depth = 3.0 km) is used in the simulation. The

synthetic seismograms computed across a vertical array (see Figure 17) are processed using the slowness analysis method (for details, see Xie et al., 2005a). Illustrated in Figure 19 are energy distributions in a mixed horizontal-slowness and depth domain (see Figure 1b), where different rows are for different combinations of source and free surface parameters and the successive frames in each row are for different time windows. The time progression allows ready identification of major phases. Phases such as Rg , pS , S^* and trapped energy from different mechanisms are labeled in the figure. Frequency filters can be applied to the synthetic data before conducting the slowness analysis. When this is viewed collectively, we know the energy distribution in combined domains of space, slowness, time and frequency. Hereafter, we will call this *SPTF* domain characterization, with the “ P ” standing for slowness.

Table 4. Source and model parameters used in numerical simulations

Group	Fixed parameters	Variables
1	$a = 0.5 \text{ km}$ $\text{Source depth} = 0.5 \text{ km}$ $Q_P = \text{infinity}$ $Q_S = \text{infinity}$	$\text{rms free surface fluctuation} =$ 0.0, 0.05, 0.10, 0.15, 0.20, 0.25, 0.30, 0.35, 0.40 km
2	$\text{rms} = 0.15 \text{ km}$ $a = 0.5 \text{ km}$ $Q_P = \text{infinity}$ $Q_S = \text{infinity}$	$\text{Source depth} =$ 0.25, 0.50, 0.75, 1.00, 1.50, 2.00, 2.50, 3.00 km
3	$\text{rms} = 0.15 \text{ km}$ $\text{Source depth} = 0.5 \text{ km}$ $Q_P = \text{infinity}$ $Q_S = \text{infinity}$	$\text{Correlation length } a =$ 0.4, 0.6, 0.8, 1.0, 2.0, 4.0, 6.0, 8.0, 10.0 km
4	$a = 0.5 \text{ km}$ $\text{Source depth} = 0.5 \text{ km}$ $Q_P = 100$ $Q_S = 50$	$\text{rms free surface fluctuation} =$ 0.0, 0.05, 0.10, 0.15, 0.20, 0.25, 0.30, 0.35, 0.40 km

In Figure 19, the solid vertical lines indicate the upper mantle S -wave slowness. Wave energy to the left of these lines has incidence angles steeper than the critical angle on the Moho and the energy will leak to the upper mantle through multiple reflections. For wave energy to the right of these lines, total reflection will keep the energy in the crustal wave guide, ultimately forming the Lg -wave at long distances (e.g. Frankel, 1989; Xie and Lay, 1994; Vogfjord, 1997; Xie et al., 2005a). Figure 19a is for a flat free surface and a relatively deep explosion source. As expected, this configuration generates neither noticeable trapped energy nor clear Rg -wave. Figure 19b is for a flat free surface and a shallow explosion source. We now see the Rg -wave developed at shallow depth and trapped energy originating from the S^* -wave (Vogfjord, 1997; Xie et al. 2005a). Figure 19c is for a deeper explosion source and a free surface with 0.15 km rms fluctuation. Comparing with 19a, the existence of a random free surface generates significant trapped

energy from surface scattering. Although the source is located at a depth of 3.0 km, R_g energy can now be seen at shallow depth. This enhanced R_g -wave comes from the free surface scattering, which can be treated as shallow secondary sources. In Figures 19d to 19f, with shallower source or larger rms free surface fluctuations, a substantial amount of trapped energy can be generated from interactions between the explosion source and the topographic fluctuations. The energy partitioned to specific regions in $SPTF$ domain can be collected and used to estimate the energy input into different regional phases. Using different source/model parameters, the relationship between these parameters and the energy partitioning processes is investigated and the underlying mechanisms revealed.

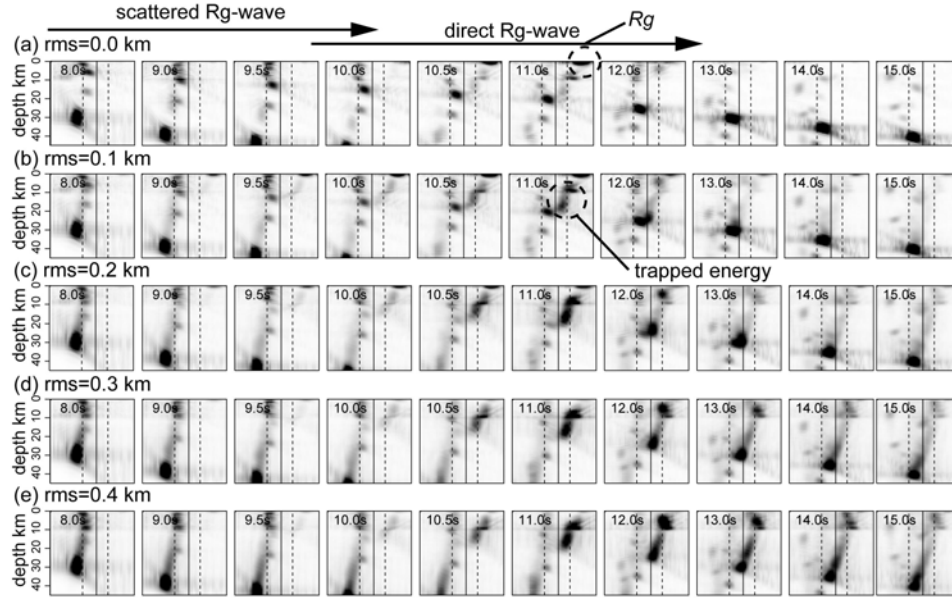


Figure 20. Slowness analysis results for models with different rms topographic fluctuations. The source depth is 0.5 km. In each time frame the horizontal coordinate is the horizontal slowness and vertical coordinate is the depth. The R_g energy is located near the surface, with slowness similar to the S-wave.

5. 2. Contributions of Free Surface Scattering to L_g -Wave Excitation

We adopt the three-layer crust (Table 2) as our basic velocity model and add random free surface fluctuations with different statistical parameters to this basic model. The random topography has an exponential power spectrum. It is located above the source and extends in both directions for 20 km. The model geometry is similar to that shown in Figure 17, with a vertical array composed of 41×90 receivers located between distances 30 and 50 km and depths 0 and 45 km. To isolate the effects of individual factors, we vary individual parameters while keeping other parameters unchanged. The varied parameters are listed in Table 4. Each model is described by a set of parameters including the rms free-surface fluctuation, the correlation length of the random power spectrum, the source depth, and the intrinsic attenuation (quality factor Q). The source depth is measured locally by taking the vertical distance between the source and the rough surface. This avoids coupled variation of depth and topographic parameters. To characterize the results statistically, we generate 10 realizations for each model. Synthetic

seismograms are calculated for each realization and processed separately. We then average the measurements from individual realizations and use their mean value as the final result for a particular case.

5.3. Effect of free surface roughness

To investigate the effect of free surface roughness on the energy partitioning, we use an infinite Q for both P - and S -waves, a source depth of 0.5 km, a correlation length of 0.5 km, and vary the rms free surface fluctuation between 0.0 and 0.4 km (see group 1 in Table 4). The slowness analysis results are illustrated in Figure 20 with different panels for models with different rms values. A frequency domain filter between 1.5 Hz and 4.0 Hz was applied to the synthetic seismograms before this slowness analysis. The Rg energy can be seen at depths less than 3 km with a slowness similar to the S -wave. In Figure 20a, with rms = 0, the Rg -wave is directly generated entirely by the explosion source. It arrives at the receiver array between 10 and 12 sec and is labeled as “direct Rg -wave”.

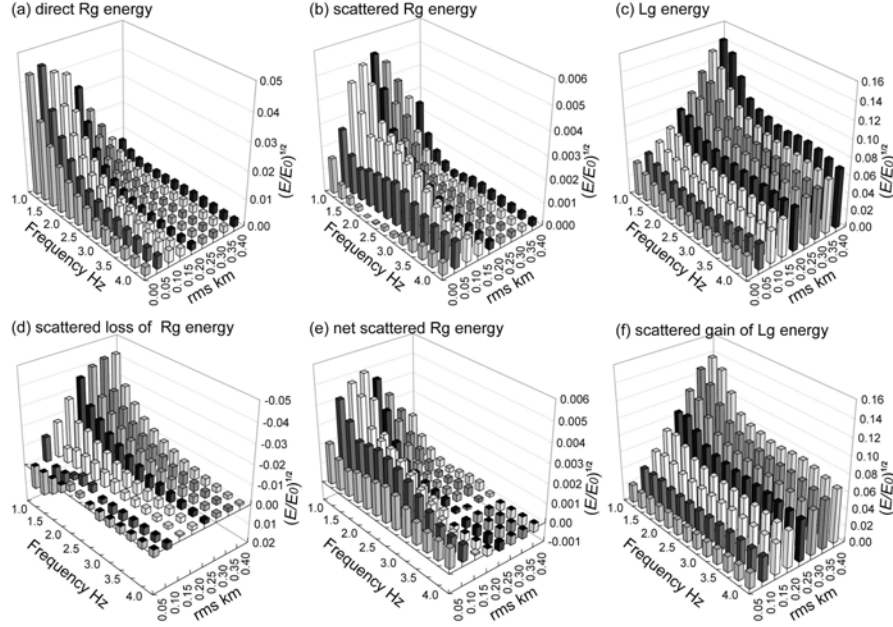


Figure 21. Responses as functions of frequency and rms free surface fluctuations. Top row: the near source responses of direct Rg , scattered Rg and the Lg -waves, with (a) R_{direct}^{Rg} , (b) R_{scatt}^{Rg} and (c) R^{Lg} . Bottom row: the contributions of surface scattering to these responses, with (d) $R_{direct}^{Rg} - R_F^{Rg}$, (e) $R_{scatt}^{Rg} - R_F^{Rg}$ and (f) $R^{Lg} - R_F^{Lg}$. Note, a negative vertical coordinate is used in (d), where the prisms with solid black tops are below zero plane, while prisms with open tops are above the zero plane.

The presence of a rough free surface causes scattering of different waves and redistributes their energy. As shallow secondary sources, the scattering generates scattered Rg -wave which can be observed in all time windows in panels 20b and 20c. The

shallow energy between 8 and 10 sec is from body wave to *Rg* scattering, as it arrives at the receiver array earlier than the direct *Rg*. We label this as “scattered *Rg*-wave” and use it to investigate body-to-surface wave scattering. Due to scattering attenuation, the same surface fluctuations that excite the scattered *Rg* can also attenuate both direct and scattered *Rg*, generating scattered body waves. In panels 20d and 20e, due to strong scattering from a very rugged free surface, both direct and scattered *Rg*-waves are very weak. Using panel 20a as a reference, the trapped energy can be quantified as a function of surface roughness.

Applying SPTF processing to the slowness analysis, we can separate the energy and estimate the excitation of different phases (Xie, et al., 2005a). A series of band pass filters is used to obtain responses between 1.0 and 4.0 Hz. Figures 21a to 21c illustrate the near-source response functions of direct *Rg*-wave, scattered *Rg*-wave and *Lg*-wave (summed trapped energy) as functions of frequency and rms surface fluctuations. The *Rg*-wave energy is obtained by picking energy peaks between depth 0 and 3 km and horizontal slowness 0.18 – 0.40 s/km. The *Lg*-wave energy is picked from peaks between depths 3 and 45 km, and slowness 0.22 – 0.40 s/km. The vertical coordinate is the square root of normalized energy. The source spectrum has been removed from the normalized energy and the results are equivalent to the response functions in equations (11) and (12). Since $E \propto f^2 A^2$, where A is the displacement amplitude, the square root of energy can be compared to the wave amplitude after being scaled with f^{-1} . For the response function R^{Rg_direct} , the energy is mainly located at low frequencies and drops quickly with increasing rms values. Note that the histogram labeled with rms = 0 indicates the response for the flat earth model. The net contribution of the surface scattering to direct *Rg*-wave can be obtained by subtracting the flat earth response from the total response (Figure 21d). The generally negative values indicate the energy loss from direct *Rg* due to the scattering attenuation, which is proportional to the rms values. Note that a negative vertical scale is used in Figure 21d, and the prisms with solid black tops are plotting below the plane zero, while prisms with open tops are plotting above the plane. At very low rms values, the *Rg*-wave gains some energy, which appears to be caused by body-to-surface wave scattering providing slightly more *Rg* energy than the energy loss from *Rg* due to scattering.

The time windows of direct and scattered *Rg*-waves partially overlap. The application of a narrow-band filter causes broadening of the *Rg* impulse and results in some leakage of direct *Rg*-wave energy into the scattered *Rg* time window (see first row in Figure 21b). By subtracting this energy, we obtain the net scattering contribution, $R^{Rg_scatt} - R_F^{Rg_scatt}$, which is shown in Figure 21e. This energy increases with increasing rms up to a moderate rms value, then decreases with further increasing rms. This suggests that small to moderate topographic fluctuations can excite secondary *Rg*-wave, but a very bumpy free surface will dramatically attenuate the short period *Rg*-wave as a consequence of both weakened excitation and strong scattering. Both low and high frequency scattered *Rg*-waves can be identified. The high frequency content falls faster with increasing rms values than its lower frequency counterpart.

Shown in Figures 21c and 21f are the Lg -wave response, R^{Lg} (i.e., summed trapped energy in the waveguide), and net scattering contribution to Lg -wave, $R^{Lg} - R_F^{Lg}$, respectively, as functions of surface topography rms value. Comparing Figures 21d and 21f, at low frequencies, the maximum scattered loss, $(E/E_0)^{1/2}$, from Rg is 0.04, while the maximum scattered gain of Lg is 0.16 at rms value 0.40 km. Assuming that all scattered loss of Rg goes to Lg , there still needs to be some Lg energy contributed from other sources, e.g., body wave scattering at the rough free surface. A broadband P -wave can excite low frequency S -waves because the surface scattering serves as shallow secondary sources. Our method cannot completely disentangle the percentage of scattered Rg going into Lg , but the evidence for significant low frequency contribution is (1) the wavefield snapshot (Figure 18d) shows considerable scattered Rg going into trapped waves, (2) the spectrum shape of energy loss of Rg is similar to the energy gain of Lg (Figures 21d and 21f), and Lg energy gain shows strong source depth dependence, as shown below. At high frequencies, Rg is weakly excited, so its scattering provides little energy for Lg -waves: most of the high frequency scattered Lg energy comes from body wave scattering.

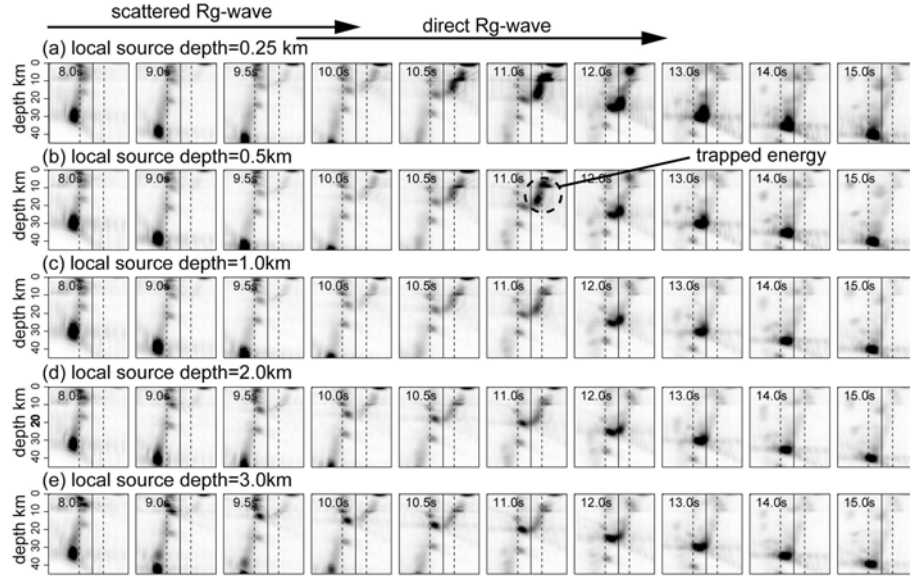


Figure 22. Similar to Figure 20 except each panel is for a different source depth.

5. 4. The Effect of Source Depth

To investigate the effect of source depth on the energy partitioning, we fix the rms free surface fluctuation at 0.15 km, the correlation length as 0.5 km and vary the source depth between 0.25 km and 3.0 km (see group 2 of Table 4). The slowness analysis results are shown in Figure 22 with each panel being for a model with a particular source depth. A prominent feature is that shallower sources generate more Rg and Lg energy. Applying the *SPTF* processing to the slowness analysis, we obtain energy response spectra for different phases. Figures 23a to 23c present the response functions of direct Rg -, scattered Rg -, and Lg -waves with respect to frequencies and source depths. With increasing source depth, the Rg energy falls quickly. Shown in Figures 23d to 23f are

separated net contributions from the free surface scattering obtained by subtracting the energy of the flat earth model from that for a random free surface. For direct Rg from a shallow source, a large amount of energy is lost due to scattering. However, for deeper sources, the scattering adds a small amount of energy to the Rg -wave (Figure 23d). The scattered Lg -wave shows an apparent increase for sources shallower than about 0.5 km which suggests a surface wave origin. The energy budget between Figures 23d and 23f are also comparable for lower frequencies and shallow sources. For Lg -wave with frequencies of 3 Hz or higher, the energy should come from body wave surface scattering.

For deeper sources, the lower frequency Lg -wave is very weak, indicating that both Rg -to- Lg and body-to- Lg conversions are weak within this frequency-depth range.

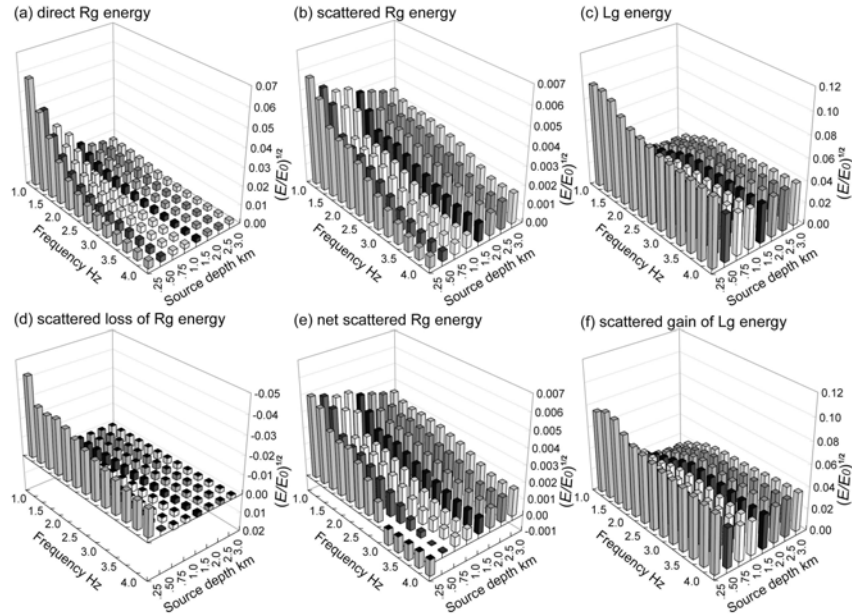


Figure 23. Similar to Figure 21, except responses are functions of frequencies and source depths. The rms surface fluctuation is 0.15 km, with correlation length 0.5 km.

5.5. The Effect of Correlation Length

To investigate the effect of correlation length on the energy partitioning, we fix the rms free surface fluctuation as 0.15 km, the source depth at 0.5 km and vary the correlation length between 0.4 km and 10 km. These parameters are listed in group 3 of Table 4. The slowness analysis results are shown in Figure 24 with each panel for a model with different correlation length. The response functions of Rg -, scattered Rg - and Lg -waves are shown in Figures 25a to 25c. The horizontal coordinate is frequency and different rows are for different correlation lengths. From these response functions, we see that the last row (for a correlation length of 10 km) is almost the same as that for a flat earth model. This indicates that a very smooth long wavelength free surface fluctuation has almost no effect on these waves. Figures 25d to 25e are net energy loss or gain from scattering. For models with correlation length shorter than 4 km, the surface scattering

apparently contributes to the generation of the trapped energy in the waveguide (Figure 25f). For very long correlation lengths, the random free surface behaves more like a flat free surface.

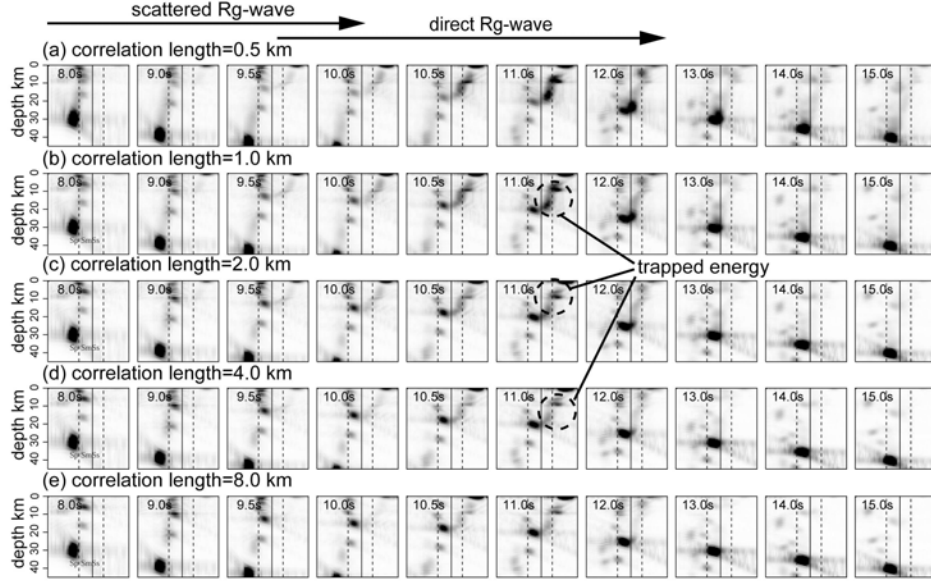


Figure 24. Similar to Figure 4 except each panel is for a model with different correlation distance.

In Figure 25f, the net scattered contribution to the Lg -wave, the response function falls with increase of the correlation length at all frequencies. For frequencies used in the simulation (1 to 4 Hz) and S -wave velocity in the top layer (3.2 km/sec), the wavelengths are between 0.8 and 3.2 km. We calculate the response as a function of normalized scale length, ka , where $k = 2\pi/\lambda$, λ is the wave length and a is the correlation length, and present the behavior in Figure 26. The maximum scattering happens around $ka = 1$ and decreases for larger ka . Extension of the calculation to smaller ka is limited by the grid size used in the boundary element calculation and the dimension of the receiver array.

5. 6. The Effect of Intrinsic Attenuation

Scattering from topographic fluctuations occurs in the uppermost crust, which is usually a low Q layer. In addition, the scattering increases the propagation distances, especially for high frequency waves. Attenuation will thus strongly affect the scattering and the overall energy distribution of an explosion source. To assess the effects of shallow attenuation, we use a set of model parameters similar to that used for testing the effect of rms fluctuations except we replace the infinite Q in the top 10 km with $Q_p = 100$ and $Q_s = 50$. These parameters are listed in group 4 of Table 4 and the results are shown in Figure 27. Comparing Figure 27 with Figure 21, two prominent features can be identified. First, compared to the purely elastic case, there is significant energy loss in the model with intrinsic attenuation. For example, the maximum amplitude (square root energy) drops approximately 35% for direct Rg -wave, 35% for scattered Rg -wave and 40% for Lg -wave. Second, the short period waves experience even larger attenuation than

long period waves. This is especially true for the scattered *Rg*-wave and the *Lg*-wave. By using low *Q* values in the calculation, our results should give fairly extreme characterization of the effect of attenuation.

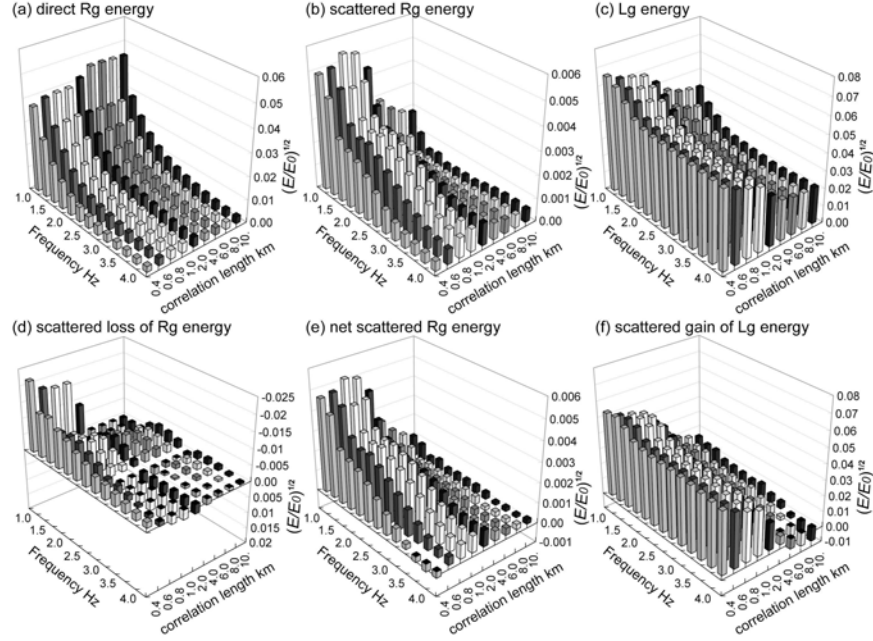


Figure 25. Similar to Figure 21, except responses are functions of frequencies and correlation lengths.

5. 7. Variance of Statistical Results

To obtain statistical relationships between the source/model parameters and the energy partitioning process, we average the measurements from individual realizations. To investigate the variance from a group of realizations with the same statistical parameters, we compare results for models with rms value 0.15 km, correlation length 0.5 km, source depth 0.5 km and infinite *Q*. The response functions for different phases are presented in Figures 28a to 28c, where the horizontal coordinates are frequency and different rows are for different realizations. The response curves for different realizations, their mean values and standard deviations are also shown in Figures 28d to 28f. The primary *Rg*-wave is relatively stable. The scattered *Rg*-wave has large variations at frequencies below about 2 Hz, while the *Lg*-wave shows large variations at frequencies above 2 Hz. Although based on the same statistical parameters, response functions from different realizations show variations in amplitudes and local minima, suggesting that the partitioning is partially affected by deterministic features very close to the source.

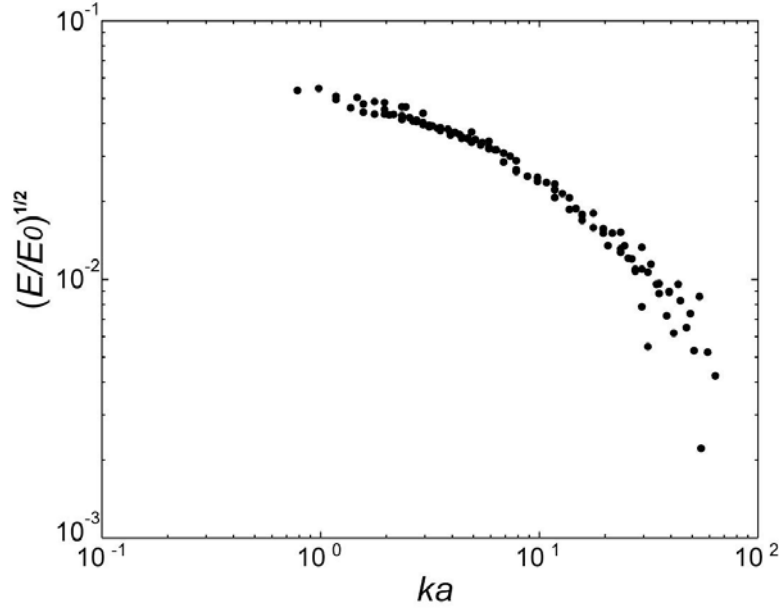


Figure 26. Net scattered Lg-energy as a function of normalized scale factor ka .

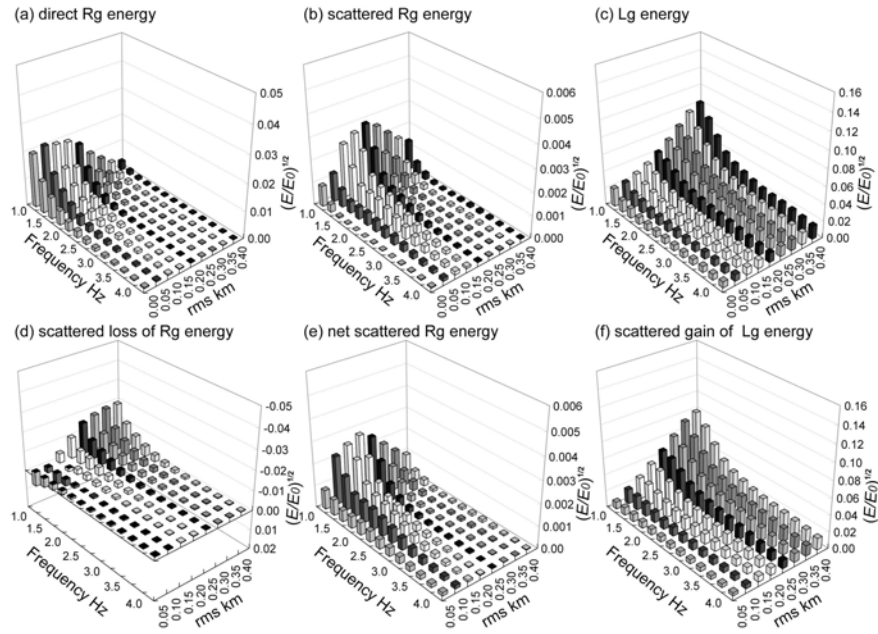


Figure 27. Similar to that shown in Figure 21, except a low Q top layer is used in the simulation. To facilitate comparison, the same vertical scale as in Figure 21 is used here.

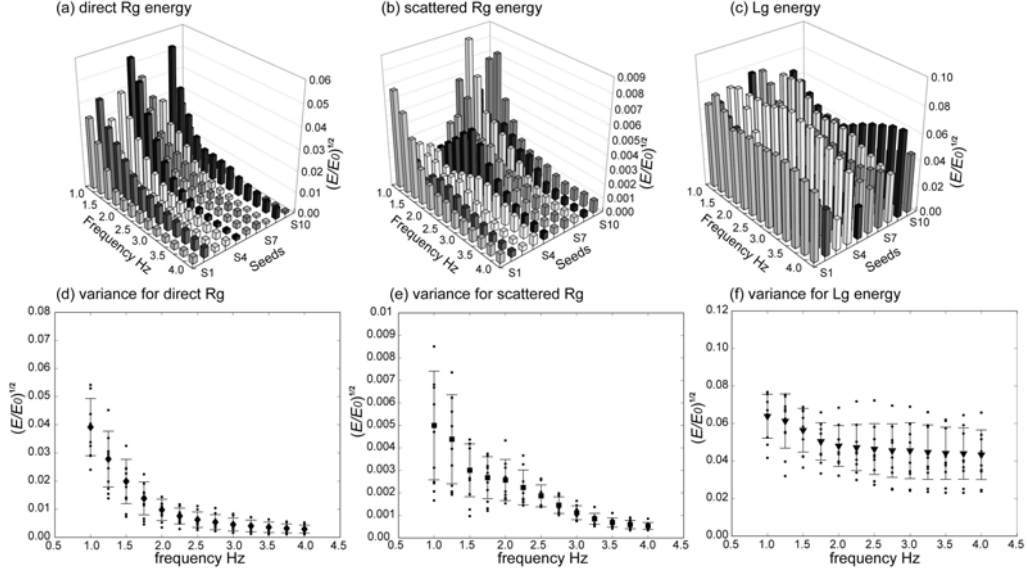


Figure 28. Top row: Responses as functions of frequencies and different random realizations, for (a) direct Rg-wave, (b) scattered Rg-wave and (c) Lg-wave. The bottom row shows response spectra from individual realizations, their mean values and standard deviations.

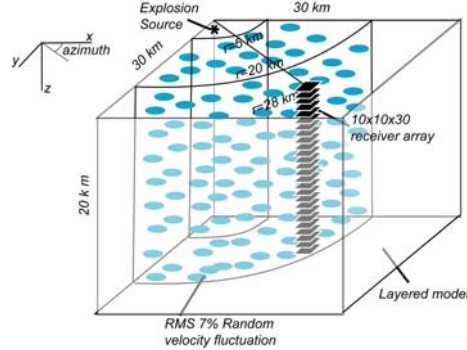


Figure 29. Cartoon showing the configuration of the 3D velocity model, source, and receiver array.

6. REGIONAL PHASE EXCITATION: SCATTERING IN THREE-DIMENSIONS

6. 1. The 3D Volumetric Scattering and Excitation of SH Component

Although most Lg observations are taken from the vertical component of seismograms, the tangential component often has as much energy as the vertical component (e.g., Stevens, et al. 2003). Some researchers pointed out that at close range, clear SH energy comparable to that on the SV component can be observed and must be generated in the source region. Any Lg-wave excitation theory must provide an explanation for these observations. Since 2D geometry decouples the P-SV problem and the SH problem, it does not provide any information on the coupling between the source and SH component. We have developed the 3D local slowness analysis method. A three dimensional velocity model is used to simulate the near source environment. The size of

the model is $30 \text{ km} \times 30 \text{ km} \times 20 \text{ km}$, and the upper crust structure from the EK model is used as the background velocity. To test the effect of the heterogeneities on the P-S coupling, 7% RMS broadband random perturbation is added to P- and S-wave velocities and the density between two cylindrical surfaces around the z-axis. An eighth-order, staggered format 3D elastic finite difference code is used to generate synthetic seismograms. The grid interval used is 0.1 km. The explosion source is located at depth 0.5 km and the dominant frequency is about 3 Hz. A $10 \times 10 \times 30$ 3D receiver array is located at epicentral distance 28 km and azimuth direction 45 degree (see Figure 29 for model configuration).

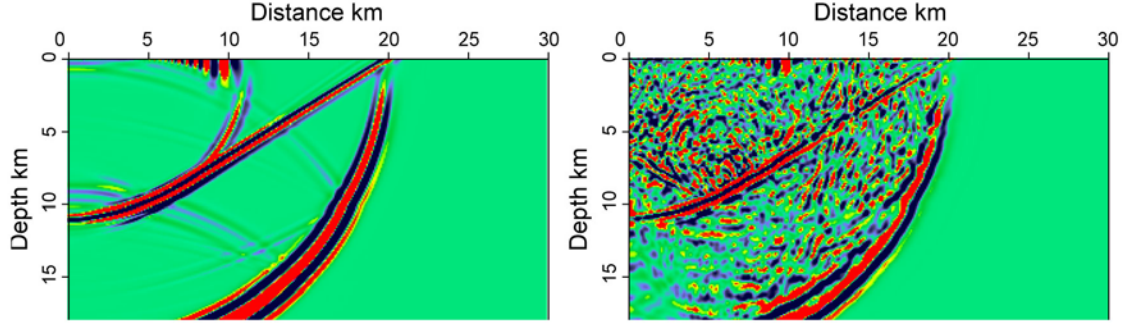


Figure 30. Wavefield snapshot for the layered background model (left) and a laterally heterogeneous model with 7% RMS random fluctuations. Shown here is the vertical component of the displacement field.

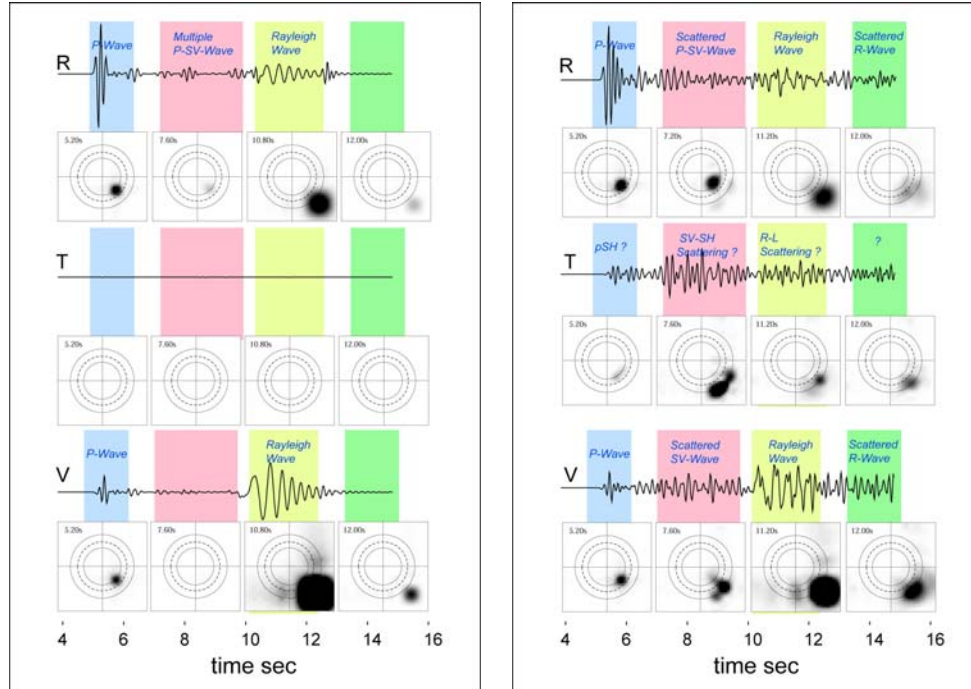


Figure 31. Comparison between synthetic seismograms and energy distribution in horizontal slowness domain for the layered velocity model (left panel) and velocity model with 7% RMS velocity fluctuations (right panel). Receivers are located at depth 1 km. All three components of the seismograms are normalized jointly but the slowness distribution for the radial component of the P-wave has

been multiplied by a factor of 0.1. The P and Rayleigh waves can be clearly seen from the radial and vertical components. Note that the tangential component for the layered model is zero. For the random velocity model, scattered waves in both the tangential and vertical components can be seen. Note that much scattered energy falls outside of the upper mantle slowness (dash line circle) and can be trapped into the crustal wave guide to form the Lg wave.

To investigate the effect of the random velocity perturbations, models both with and without the random fluctuations are calculated and their wavefield snapshots are shown in Figure 30. No surface roughness is included here. Scattered energy appears in the model with random velocity fluctuations. Shown in Figures 31 are synthetic seismograms and the 2D horizontal slowness analysis from selected time windows for both the background and random models. The source depth is 0.5 km and receiver arrays are located at depth 1 km. For the background model (left panel), the P and Rayleigh waves can be clearly seen. Note the tangential component is zero. All three components of the seismograms are normalized jointly, but the slowness distribution for the radial component of the P-wave has been multiplied by a factor of 0.1. For the random model with 7% RMS velocity fluctuations (right panel), there are scattered waves in all three components including the tangential (SH) component. Much of the scattered energy falls outside of the upper mantle slowness (dashed line circle) and can thus be trapped into the crustal waveguide to form the regional phases.

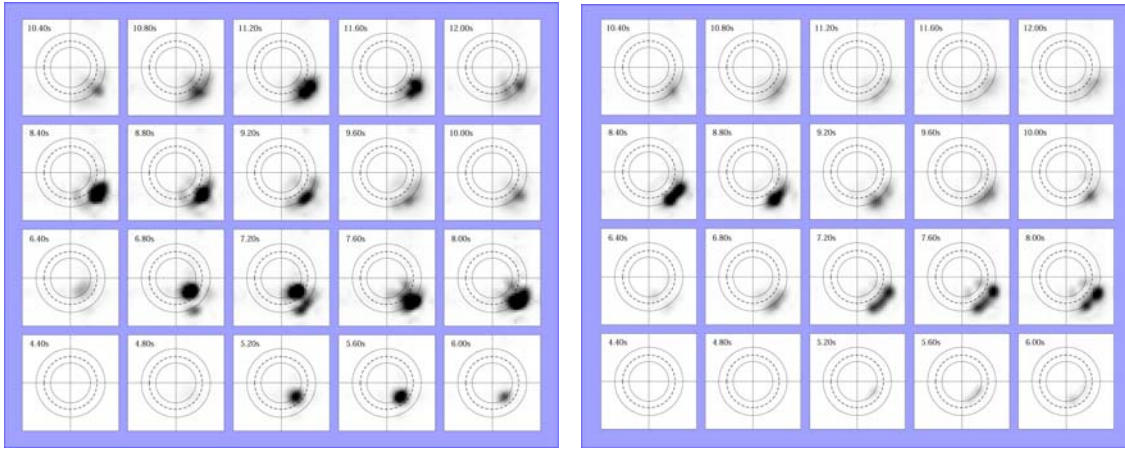


Figure 32. The wave energy distribution in the 2D horizontal slowness domain for the vertical (left) and tangential (right) components. The receiver array is located at epicentral distance 28 km and depth 7 km. Note the energy distribution outside of the upper mantle S-wave velocity.

Figure 32 gives the 2D horizontal slowness analysis for vertical and tangential components for the random velocity model. The receiver array is located at depth 7 km and epicentral distance 28 km. In the left panel for the vertical component, we can see that both P-wave (around 5.2 s to 5.6 s) and pS-wave (around 6.8 to 7.2 s) share the same slowness and will not contribute to the guided wave mode. Within the time window between 7.2 and 9.2 s, there is scattered P-SV energy propagating with a larger apparent horizontal slowness. The energy falls beyond the upper mantle S-wave slowness and will

be trapped in the waveguide to form the P-SV Lg wave. In the right panel for the tangential component, there is considerable SH type scattered energy between 7.2 and 9.2 s with slowness greater than the upper mantle S-wave slowness. The following features can be found from the results: (1) There is considerable SH energy excited due to the near source lateral heterogeneities; (2) The SH energy appears to be generated through P-pS-SH or SV-SH since the SH component is relatively weak immediately following the P-wave front. The scattered energy has a broader azimuth range than the direct arrivals, which may provide a hint to reveal the actual scattering mechanisms. (3) Both SV and SH scattered energy can fall into the proper slowness region and form the crustal guided wave.

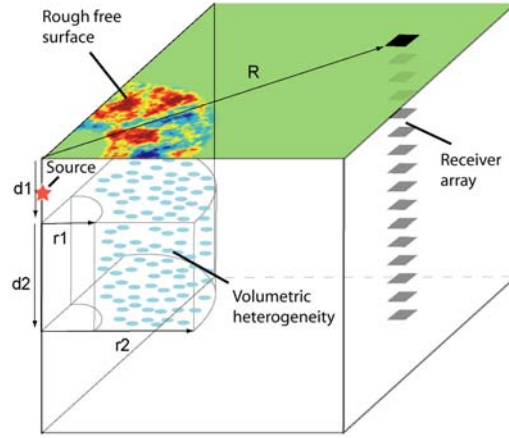


Figure 33. The 3D velocity model including both irregular free surface and volumetric heterogeneity (shown here is one quarter of the model). The rough topography is located between distances 5 km and 15 km. The volumetric heterogeneity is located between distances 5 km and 15 km, and between depths 1 km and 5 km. The synthetic seismograms are collected from a 3D array located at epicentral distance 28 km.

6. 2. The 3D Simulation Including both Rough Free Surface Scattering and Volumetric Scattering

To include both volumetric heterogeneity and irregular topography in a 3D simulation and investigate their effects on near source energy partitioning, we use the 3D finite-difference method developed by Zhang and Chen (2006). In this finite-difference algorithm, the physical domain is discretized by boundary-conforming grids. The irregular surface is transformed into a ‘flat’ surface in computational space, thus avoiding the artifact usually caused by using the staircase approximation. To satisfy the free surface boundary conditions, the method uses the stress image method on the irregular topography. With this method, approximately 10 grid points per shortest wavelength is usually enough to maintain the global accuracy of the simulation. For simulation, we use a $60\text{ km} \times 60\text{ km} \times 30\text{ km}$ velocity model (grid size $600 \times 600 \times 300$). Shown in Figure 33 is one quarter of the model. An explosion source is located at the center of the model with a depth of 0.5 km. The rough topography is located between epicenter distances 5 and 15 km. The volumetric heterogeneity is located between horizontal distances 5 and 15 km

and between depths 1 km and 5 km. A $N_x \times N_y \times N_z = 10 \times 10 \times 16$ (4 km \times 4 km \times 30 km) receiver array located at epicenter distance 28 km is used to collect the synthetic seismograms.

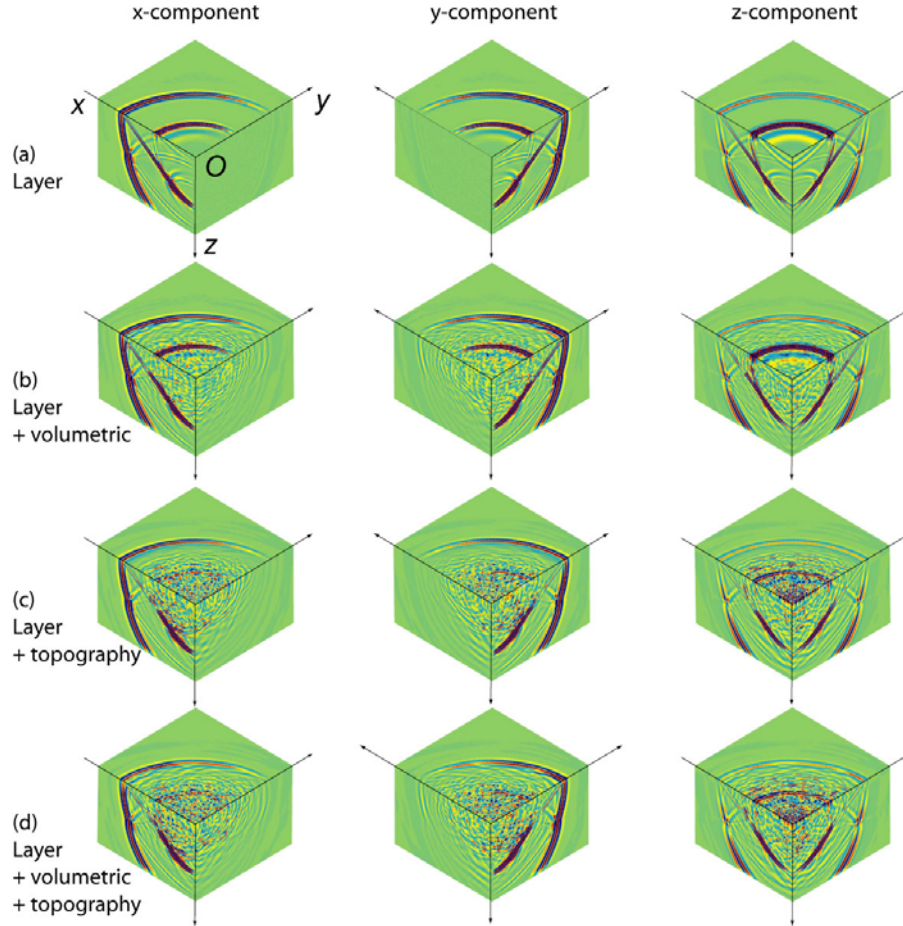


Figure 34. Snap shots for an explosion source in different velocity models. Rows (a) to (d) are for a layered model, a layered model with volumetric random velocity fluctuation, a layered model with irregular topography, and a layered model with both volumetric heterogeneity and random topography. The three columns are for x-, y- and z-components.

Shown in Figure 34 are snapshots for an explosion source in different velocity models. From rows (a) to (d) are for a layered model, a layered model with volumetric random velocity fluctuation, a layered model with irregular topography, and a layered model with both volumetric heterogeneity and random topography. The three columns are for x-, y- and z-components. The rough surface has an exponential power spectrum, a rms fluctuation of 0.2 km, and a correlation distance of 2.0 km. The volumetric heterogeneity has an exponential power spectrum, a rms perturbation of 5%, and a correlation length of 2.0 km. For a layered model shown in row (a), an explosion source generates P, pS, Rg and some interface reflections, which are all P-SV waves. As

examples, we see the x-component is zero in plane yOz and y-component is zero in plane xOz . For models with volumetric and/or rough topography, i.e., rows (b) to (d), there are apparent scattered waves following the primary phases. Particularly, SH-waves appear in tangential component, e.g., the non-zero x-component in yOz plane and non-zero y-component in xOz plane.

Shown in Figure 35 are synthetic seismograms and slowness analysis for (a) a layered crustal model and (b) a layered model plus free surface and volumetric heterogeneity. The model geometry is shown in Figure 33. The top, middle and bottom rows are for radius, tangential and vertical components, respectively. The rough surface has an exponential power spectrum, a rms fluctuation of 0.2 km and a correlation distance of 2.0 km. The volume heterogeneity has a 5% velocity perturbation, an exponential power spectrum and a correlation length of 2 km. The synthetic seismograms are filtered between 0.5 and 5.0 Hz and normalized using the same scale. The horizontal distance from the source to the center of the receiver array is about 28 km. The 2D slowness analyses are conducted in horizontal plane (the map view) for phases P, PP, PS, Rg and coda waves. The results show that for an explosion source in a layered model, there is no SH wave and the energy is distributed within the upper mantle S wave slowness (the dashed circle). For a model with both rough free surface and the volumetric heterogeneity, the primary P and Rg waves are strongly attenuated due to the scattering. From slowness analysis, there are both SV and SH waves with their slowness distributed outside the upper mantle S-wave slowness, indicating part of their energy has been trapped in the crustal waveguide to form the Lg-wave.

6.3. The Lg excitation Caused by the 3D Surface Scattering

We further investigate the effect of 3D surface scattering on the excitation of Lg wave. We use a model configuration similar to that shown in Figure 33. The correlation length of the surface random topography is 2.0 km and the rms fluctuation is 0.15 km. A 2.5 Hz Ricker wavelet is used in the simulation. We first conduct the local slowness analysis and calculate the energy distribution in horizontal slowness domain (p_x, p_y) at different depths (similar to that shown in Figure 1d). Then we integrate the energy in the (p_x, p_y) domain along the equal slowness circles and obtain the energy distribution as a function of horizontal slowness and depth. We calculate and compare the energy distribution for the layered EK model, EK model plus Gaussian random topography and EK model plus exponential random topography.

Shown in Figure 36 is for the EK model. Similar to that in the 2D case (see Section 5), in a model with high velocity top layer, the energy of pP wave is mostly distributed to the left of the upper mantle S-slowness. The weak Lg wave (trapped energy) is generated from the S^* phase. The Rg wave can be seen at the shallow part of the model. There is no energy partitioned to the tangential component. Shown in Figure 37 is for the EK model plus the Gaussian random topography. We see part of the energy is transferred from P-SV mode to the SH mode. A Gaussian random surface model is mostly composed of smoothly varying fluctuations which generate weak scattering. The

Rg wave is weakened but the Love type wave is generated at the shallow crust. Shown in Figure 39 is for the EK model plus the exponential random topography. Comparing to a Gaussian random model, an exponential random model contains more small scale topographic fluctuations which tends to deflect more energy towards wide-angle scattering, thus is more effective in transmit energy in the slowness domain. The scattered energy can be clearly observed following the pS wave front in both P-SV and SH mode. There is more energy being shifted across the upper mantle S-slowness and being trapped in the waveguide. Generally, a model with more small scale topographic fluctuations tends to generate more trapped energy.

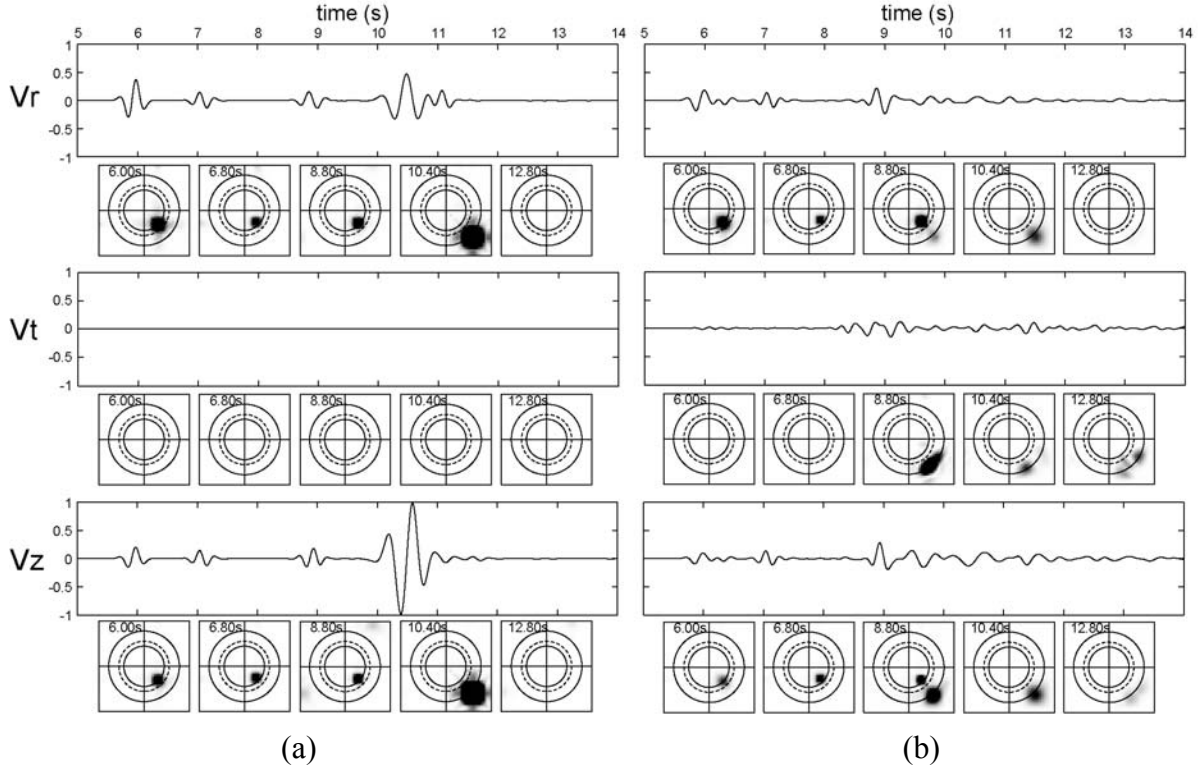


Figure 35. Synthetic seismograms and slowness analysis for (a) a layered crustal model and (b) a layered model with rough free surface and volumetric heterogeneity. The model geometry is shown in Figure 33.

By applying time windows to the successive time frames in Figures 36-38 and summing up the energy within time windows, we obtain energy for different phases as well as for different components. Table 5 lists the normalized energy for Rg and Lg waves from different topographic models. We see that the layered EK model has large Rg energy but very weak Lg energy. The energy for tangential component is zero. For models with random topographic fluctuations, the Rg wave loses energy but the Lg wave gains energy. There is energy transferred from the P-SV mode to the SH mode as well. An exponential random model, which has more small scale fluctuations, appears to provide more efficient coupling compared to a Gaussian random model. The above results may suggest that part of the Rg energy is transferred into the Lg energy through the surface scattering. However, the body wave energy, which has not been investigated here, may also contribute to this process.

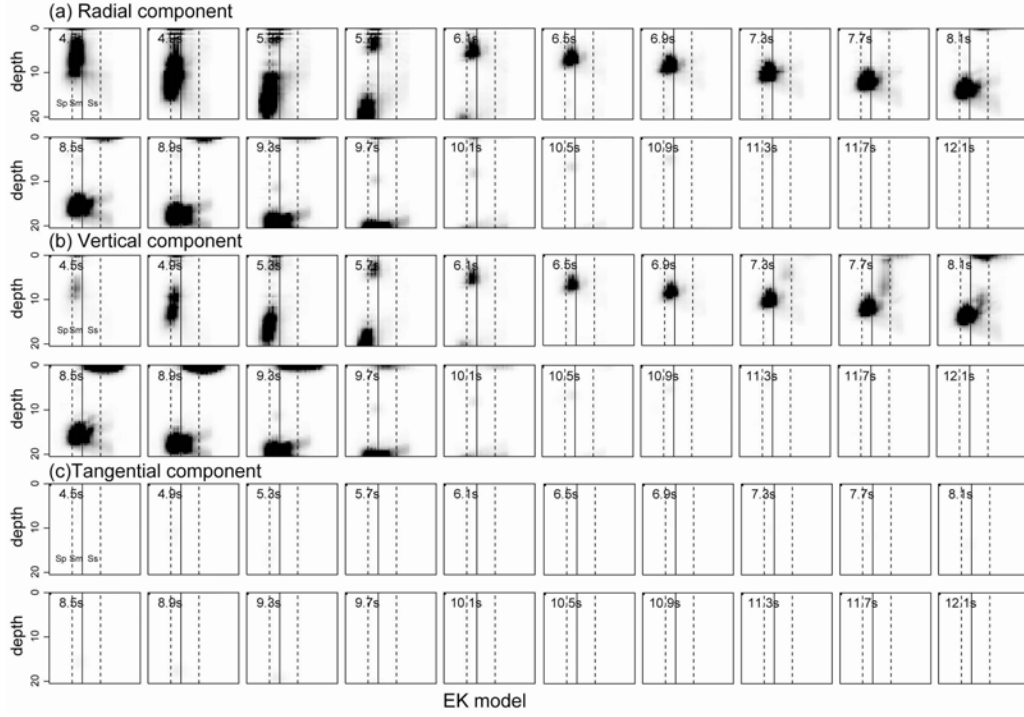


Figure 36. Wave energy in horizontal slowness and depth domain in the EK model.

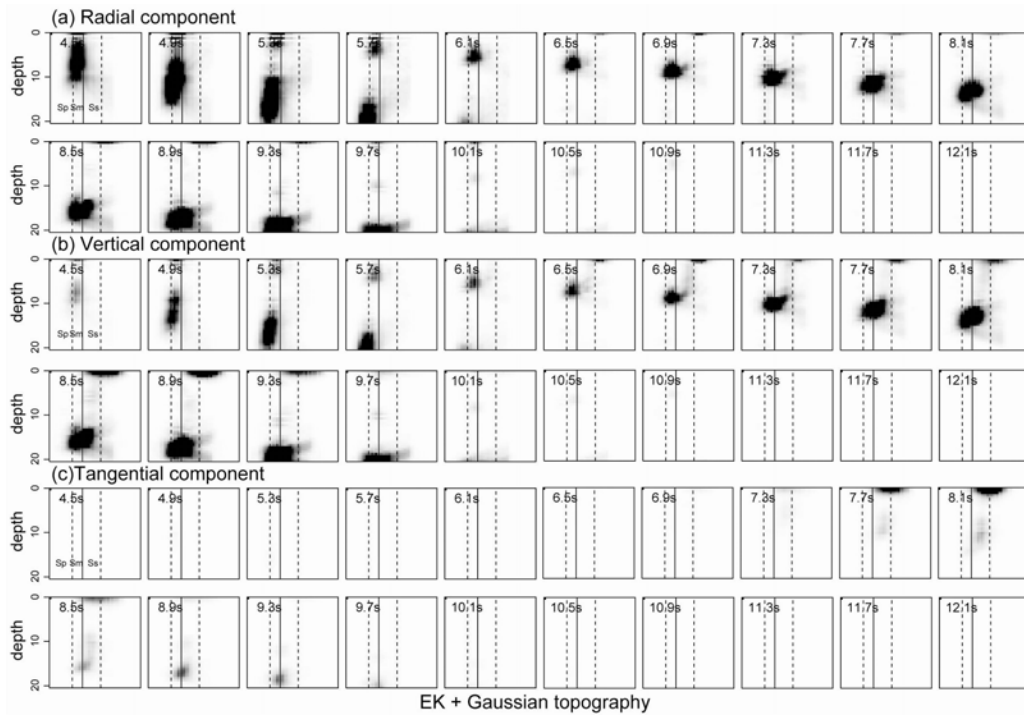


Figure 37. Wave energy in horizontal slowness and depth domain in EK model plus free surface rough topography. The random free surface has a Gaussian power spectrum.

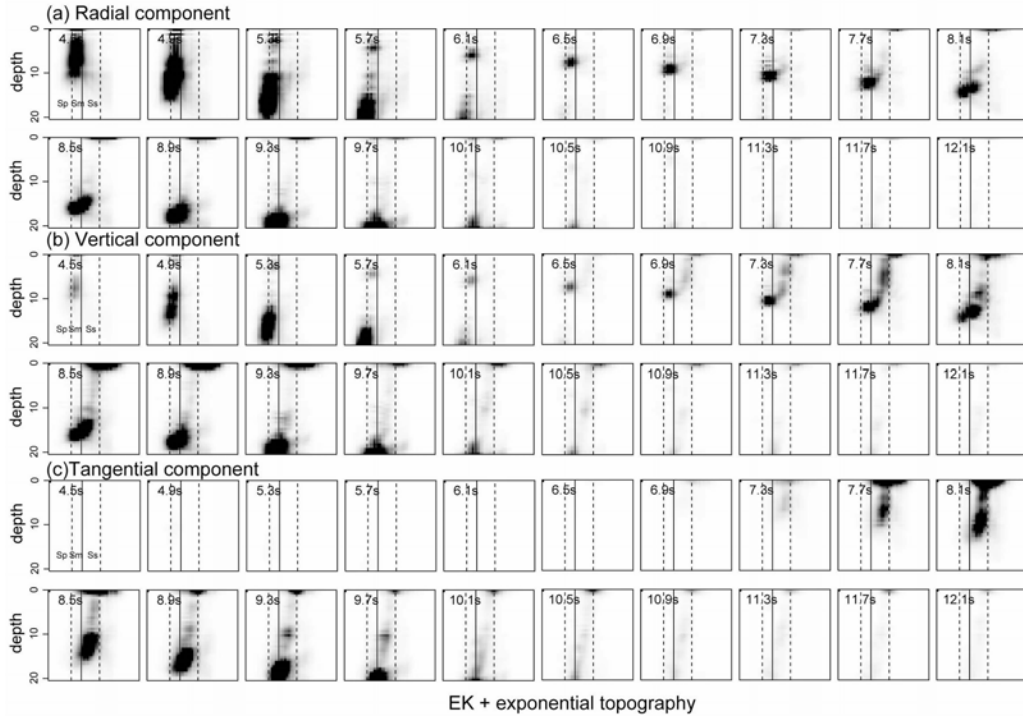


Figure 38. Wave energy in horizontal slowness and depth domain in EK model plus free surface rough topography. The random free surface has an exponential power spectrum.

Table 5. Normalized energy E/E_0 for Rg and Lg waves in different random surface models.

Waves and components		EK model	EK model plus Gaussian topography	EK model plus exponential topography
Rg	H	5.4×10^{-9}	1.1×10^{-9}	1.6×10^{-9}
	V	2.3×10^{-8}	4.0×10^{-9}	7.0×10^{-9}
	T	0	2.8×10^{-9}	1.0×10^{-8}
	Energy	2.8×10^{-8}		
	Compare to EK		-2.0×10^{-8}	-9.0×10^{-9}
Lg	H	2.8×10^{-9}	5.5×10^{-9}	4.3×10^{-9}
	V	3.5×10^{-9}	1.1×10^{-8}	8.6×10^{-9}
	T	0	1.1×10^{-9}	2.0×10^{-8}
	Energy	6.3×10^{-9}		
	Compare to EK		$+1.1 \times 10^{-8}$	$+2.7 \times 10^{-8}$

7. CONCLUSION

We use 2D and 3D finite-difference method and 2D boundary-element method to simulate the scattering in the near-source environment. A local slowness analysis method is developed to investigate near-source energy partitioning and *Lg*-wave excitation for explosive sources. The method has two major advantages. First, it allows us to study the near-source processes in multiple domains including space, time, slowness and frequency. This provides an opportunity to isolate different mechanisms within the complex near-source environment. Second, this method can be applied at a close range, well before the *Lg*-wave is actually formed. It provides us with uncontaminated near-source information by calculating a relatively small velocity model with very fine near-source structures. Since this is a very efficient method, we can use it to investigate a broad frequency band and to test a large number of source-model parameters.

We investigate the contributions of *P*-*pS*-to-*Lg* conversion and *S**-to-*Lg* excitation using 2D finite-difference method and models with near-source random velocity fluctuations. The results show that the near source scattering plays an important role in generating the *Lg* wave from an explosion source. The contribution of *S**-to-*Lg* is concentrated at low frequencies and occurs for very shallow source depths. The contribution of *P*-*pS*-to-*Lg* coupling in the presence of near-source small-scale random heterogeneities is concentrated at high-frequencies. The excitation spectra of these mechanisms are calculated.

We use the 2D boundary-element simulation to investigate the effect of topographic scattering on the near-source energy partitioning for an explosion source. Random topographic models with different statistical properties, variable source depth, and different *Q* models are included in the investigation. The responses of different phases as functions of frequency and source/model parameters are calculated and their energy budget evaluated. The results reveal that free surface scattering has strong effect on near source energy partitioning. The scattering process can excite the *Rg*-wave for a moderately rugged topography, but dramatically attenuates short period *Rg*-waves when the surface becomes too rugged. For models with a high velocity shallow crust, the free surface scattering provides an important mechanism that transfers energy for an explosion source into the *Lg*-wave in the near source region. At lower frequencies and for a moderately rugged free surface, the *Rg*-to-*Lg* transfer is relatively efficient. At higher frequencies and for a very rugged free surface, the body-to-*Lg* transfer may dominate the process. The correlation length of the random free surface fluctuation provides specific frequency dependence to the transfer function, with maximum coupling near $ka=1$. Intrinsic attenuation within the uppermost crust has a strong effect on the energy transfer through surface scattering, with high frequency content losing energy faster than the lower frequency waves.

We expand our simulation and analysis to fully 3D models with both volumetric heterogeneity and rough free surface. Investigating the near source process in 3D is more realistic because it gives correct scattering pattern and geometric spreading. In addition, a general 3D model provides the coupling between the *P*-*SV* and *SH* waves. Velocity

models with different volume heterogeneities and surface fluctuations are tested and compared. For an isotropic explosion source in a typical layered model with high velocity top layer, only weak Lg wave (trapped guided wave) can be generated from the S^* phase. There is no energy in the tangential component. When adding volume heterogeneities or surface fluctuations in the model, the energy transfers from leaky mode to trapped guided waves as well as from P-SV mode to the SH mode. For the surface scattering, an exponential random surface fluctuation provide stronger coupling than a Gaussian random surface model. Generally, a model with more small scale topographic fluctuations tends to generate more trapped energy.

REFERENCES

- Bonner, J.B., H.J. Patton, A.C. Rosca, H. Hooper, J. Orrey, M. Leidig and I. Gupta (2003). Aspects of Rg and Lg generation from the Shagan depth of burial explosions, in *Proceedings of the 25th Seismic Research Review, Nuclear Explosion Monitoring: Building the Knowledge Base*, 384-394.
- Bottone, S., M.D. Fisk, and G.D. McCartor (2002). Regional seismic event characterization using a Bayesian formulation of simple kriging, *Bull. Seism. Soc. Am.* 92, 2277-2296.
- Bradley, C.R. and E.M. Jones (1998). Modeling propagation effects from explosion in Western China and India, in *Proceedings of the 20th Annual Seismic Research Symposium on Monitoring a Comprehensive Nuclear-Test-Ban Treaty*, 173-181.
- Bradley, C.R. and L.E. Jones (1999). Full waveform modeling of the effects of Q and structure over sub-regional paths, in Western China, in *Proceedings of the 21st Annual Seismic Research Symposium on Monitoring a Comprehensive Nuclear-Test-Ban Treaty*, 28-38.
- Day, S.M. and K.L. McLaughlin (1991). Seismic source representations for spall, *Bull. Seism. Soc. Am.* 81, 191-201.
- Fan, G.W. and T. Lay (1998a). Statistical analysis of irregular waveguide influences on regional seismic discriminants in China, *Bull. Seism. Soc. Am.* 88, 74-88.
- Fan, G.W. and T. Lay (1998b). Regionalized versus single-station wave-guide effects on seismic discriminants in western China, *Bull. Seism. Soc. Am.* 88, 1260-1274.
- Fan, G.W. and T. Lay (1998c). Statistical analysis of irregular waveguide influences on regional seismic discriminants in China: additional results for Pn/Sn, Pn/Lg and Pg/Sn, *Bull. Seism. Soc. Am.* 88, 1504-1510.
- Fisk, M. D., H. L. Gray, and G. D. McCartor (1996). Regional discrimination without transporting thresholds, *Bull. Seism. Soc. Am.* 86, 1545-1558.
- Fisk, M. D. (2006). Source spectral modeling of regional *P/S* discriminants at nuclear test sites in China and the former Soviet Union, *Bull. Seism. Soc. Am.* 96, 2348-2367.
- Frankel, A. (1989). A review of numerical experiments on seismic wave scattering, in *Scattering and Attenuation of Seismic Waves, II*, edited by R.S. Wu and K. Aki, pp. 639-686, Birkhauser, Berlin.
- Ge, Z., L. Y. Fu and R. S. Wu (2005). *P-SV* Wavefield connection technique for regional wave propagation simulation, *Bull. Seism. Soc. Am.* 95, 1375-1386.
- Gupta, I.N., W. Chan, and R. Wagner (1992). A comparison of regional phases from underground nuclear explosions at East Kazakh and Nevada Test Sites, *Bull. Seism. Soc. Am.* 82, 352-382.
- Gupta, I.N., T. Zhang, and R.A. Wagner (1997). Low-frequency Lg from NTS and Kazakh nuclear explosions: observations and interpretations, *Bull. Seism. Soc. Am.* 87, 1115-1125.

- Gupta, I. N., W. W. Chan, and R. A. Wagner (2005). Regional source discrimination of small events based on the use of *Lg* wavetrain, *Bull. Seism. Soc. Am.*, **95**, 341-346.
- Gutowski, P.R., F. Hron, D.E. Wagner, and S. Treitel (1984). *S**, *Bull. Seism. Soc. Am.* **74**, 61-78.
- Hartse, H. E., S. R. Taylor, W. S. Phillips, and G. E. Randall (1997). A preliminary study of regional seismic discrimination in central Asia with emphasis on western China, *Bull. Seism. Soc. Am.*, **87**, 551-568.
- He, Y., X.B. Xie, and T. Lay, 2008, Explosion source energy partitioning and *Lg*-wave excitation: contributions of free surface scattering, *Bull. Seism. Soc. Am.*, **98**, 778-792.
- Hong, T. K., and J. Xie (2005). Phase composition of regional seismic waves from underground nuclear explosions, *J. Geophys. Res.*, **110**, (B1), 2303, doi:10.1029/2005JB003753.
- Jih, R.S. (1995). Numerical investigation of relative contribution of *Rg* scattering and incomplete dissipation to *Lg* excitation, in *Proceedings of the 17th Annual Seismic Research Symposium on Monitoring a Comprehensive Nuclear-Test-Ban Treaty*, 401-410.
- Jih, R.S. (1996). Waveguide Effects of large-scale structural variation, anelastic attenuation, and random heterogeneity on SV *Lg* propagation: a finite-difference modeling study, in *Proceedings of the 18th Annual Seismic Research Symposium on Monitoring a Comprehensive Nuclear-Test-Ban Treaty*, 182-194.
- Johnson, L.R. and C.G. Sammis (2001). Effects of rock damage on seismic waves generated by explosions, *Pageoph*, **158**, 1869-1908.
- Kennett, B.L.N. (1989). *Lg*-wave propagation in heterogeneous media, *Bull. Seism. Soc. Am.* **79**, 860-872.
- Kennett, B.L.N. and S. Mykkeltveit (1984). Guided wave propagation in laterally varying media, II. *Lg* wave in northwestern Europe, *Geophys. J. R. Astr. Soc.* **79**, 257-267.
- Kim, W.Y., V. Aharonian, A. L. Lerner-Lam, and P.G. Richards (1997). Discrimination of earthquakes and explosions in southern Russia using regional high-frequency three-component data from IRIS/JSP Caucasus Network, *Bull. Seism. Soc. Am.* **87**, 569-588.
- Kim, W.Y., D.W. Simpson, and P.G. Richards (1993). Discrimination of earthquakes and explosions in the eastern United States using regional high-frequency data, *Geophys. Res. Lett.* **20**, 1507-1510.
- Lilwall, R.C., (1988). Regional *m_b*:*M_s*, *Lg*/*Pg* amplitude ratios and *Lg* spectral ratios as criteria for distinguishing between earthquakes and explosions: a theoretical study, *Geophys. J. Int.*, **93**, 137-147.
- McLaughlin, K. L., and R. S. Jih (1988). Scattering from near-source topography: Teleseismic observations and numerical simulations, *Bull. Seism. Soc. Am.* **78**, 1399-1414.

- Myers, S. C., W. R. Walter, K. Mayeda, and L. Glenn (1999). Observations in support of *Rg* scattering as a source for explosion *S* waves: Regional and local recordings of the 1997 Kazakhstan depth of burial experiment, *Bull. Seism. Soc. Am.* **89**, 544-549.
- Myers, S.C., J. Wagoner, S. Larsen, A. Rodgers, K. Mayeda, K. Smith, and W. Walter (2003). Simulation of regional explosion S-phases (SIREs) project, in *Proceedings of the 25th Seismic Research Review, Nuclear Explosion Monitoring: Building the Knowledge Base*, 117-124.
- Myers, S. C., J. Wagoner, L. Preston, K. Smith, and S. Larsen (2005). The effect of realistic geologic heterogeneity on local and regional *P/S* amplitude ratios based on numerical simulations, in *Proceedings of the 27th Seismic Research Review: Ground-Based Nuclear Explosion Monitoring Technologies*, 123-132.
- Nuttli, O.W. (1986). Yield estimates of Nevada Test Site explosions obtained from *Lg* waves, *J. Geophys. Res.* **91**, 2137-2151.
- Priestley, K. F., G. Zandt, and G. E. Randall (1988). Crustal structure in Eastern Kazakh, USSR from teleseismic receiver functions, *Geophys. Res. Lett.* **15**, 613-616.
- Patton, H. J., and S. R. Taylor (1995). Analysis of *Lg* spectral ratios from NTS explosions: implications for the source mechanisms of spall and the generation of *Lg* waves, *Bull. Seism. Soc. Am.* **85**, 220-236.
- Patton, H.J. (2001). Regional magnitude scaling, transportability, and *Ms:mb* discrimination at small magnitudes, *Pageoph*, **158**, 1951-2015.
- Sato, H. and M.C. Fehler (1998). *Seismic Wave Propagation and Scattering in the Heterogeneous Earth*, Springer-Verlag New York, Inc.
- Stevens, J.L., G.E. Baker, H. Xu, T.J. Bennett, N. Rimer, and S.M. Day (2003). The physical basis of *Lg* generation by explosion sources, in *Proceedings of the 25th Seismic Research Review, Nuclear Explosion Monitoring: Building the Knowledge Base*, 456-465.
- Stevens, J. L., G. E. Baker, H. Xu, T. J. Bennett (2005). The physical basis of the explosion source and generation of regional seismic phases, in *Proceedings of the 27th Seismic Research Review: Ground-Based Nuclear Explosion Monitoring Technologies*, 663-672.
- Taylor, S.R. (1996). Analysis of high frequency *Pn/Lg* ratios from NTS explosions and western U.S. earthquakes, *Bull. Seism. Soc. Am.* **86**, 1042-1053.
- Taylor, S.R., M.D. Denny, E.S. Vergino, and R.E. Glaser (1989). Regional discrimination between NTS explosions and western U.S. earthquakes, *Bull. Seism. Soc. Am.* **79**, 1142-1176.
- Taylor, S. R. (1996). Analysis of high frequency *Pn/Lg* ratios from NTS explosions and western U.S. earthquakes, *Bull. Seism. Soc. Am.* **86**, 1042-1053.
- Taylor, S. R., M. D. Denny, E. S. Vergino, and R. E. Glaser (1989). Regional discrimination between NTS explosions and western U.S. earthquakes, *Bull. Seism. Soc. Am.* **79**, 1142-1176.

- Taylor, S.R. and H.E. Hartse (1997). An evaluation of generalized likelihood ratio outlier detection to identification of seismic events in Western China, *Bull. Seism. Soc. Am.* 87, 824-831.
- Vogfjord, K.S. (1997). Effects of explosion depth and earth structure on the excitation of Lg waves: S* revisited, *Bull. Seism. Soc. Am.* 87, 1100-1114.
- Wallace, T.C. (1991). Body wave observations of tectonic release, in: S.R. Taylor, H.J. Patton and P.G. Richards (editors), *Explosion Source Phenomenology*, pp 161-170, American Geophysical Union.
- Walter, W.R., K.M. Mayeda, and H. Patton (1995). Phase and spectral ratio discrimination between NTS earthquakes and explosions, Part I: Empirical observations, *Bull. Seism. Soc. Am.* 85, 1050-1067.
- Wu, R.S. and K. Aki (editor), (1988). *Scattering and Attenuation of Seismic Waves, Volume I*, Birkhauser Verlag, Boston.
- Wu, R.S., S. Jin and X.B. Xie (2000a). Seismic wave propagation and scattering in heterogeneous crustal waveguides using screen propagators: I SH waves, *Bull. Seism. Soc. Am.* 90, 401-413.
- Wu, R.S., S. Jin and X.B. Xie (2000b). Energy partition and attenuation of Lg waves by numerical simulations using screen propagators, *Phys. Earth and Planet. Inter.* 120, 227-243.
- Wu, R. S., X. B. Xie, Z. Ge, X. Wu, and T. Lay (2003). Quantifying source excitation and path effects for high-frequency regional waves, in *Proceedings of the 25th Seismic Research Review, Nuclear Explosion Monitoring: Building the Knowledge Base*, 172-181.
- Xie, J. (2002). Source scaling of Pn and Lg spectra and their ratios from explosions in central Asia: Implications for the identification of small seismic events at regional distances, *J. Geophys. Res.* 107, B7, 10.1029/2001JB000509.
- Xie, J., L.L. Cong, and B.J. Mitchell (1996). Spectral characteristics of the excitation and propagation of Lg from underground nuclear explosions in central Asia, *J. Geophys. Res.* 101, 5813-5822.
- Xie, X.B. and T. Lay (1994). The excitation of Lg waves by explosions: A finite-difference investigation, *Bull. Seism. Soc. Am.* 84, 324-342.
- Xie, X. B., Z. Ge and T. Lay (2005a). Investigating explosion source energy partitioning and Lg-wave excitation using a finite-Difference plus slowness analysis method, *Bull. Seism. Soc. Am.* 95, 2412-2427.
- Xie, X. B., T. Lay, and R. S. Wu (2005b). Near source energy partitioning for regional waves in 2D and 3D models, contributions of S*-to-Lg and P-to-Lg scattering, in *Proceedings of the 27th Seismic Research Review: Ground-based Nuclear Explosion Monitoring Technologies*, 249-258.
- Xie, X.B., T. Lay, R.S. Wu, and Y. He, 2006, Near source energy partitioning for regional waves in 2d and 3d models, contributions of free surface scattering,

Proceedings of the 28th Seismic Research Review: Ground-based Nuclear Explosion Monitoring Technologies, 304-314.

Xie, X.B., T. Lay, R.S. Wu, and Y. He, 2007, Near source energy partitioning for regional waves in 2d and 3d models, effects from random free surface scattering, *Proceedings of the 29th Monitoring Research Review: Ground-based Nuclear Explosion Monitoring Technologies*, 322-332.

Zhang, W., and X. Chen (2006). Traction image method for irregular free surface boundaries in finite difference seismic wave simulation, *Geophys. J. Int.*, 167, 337–353.

